AD_____

Award Number: DAMD17-02-1-0516

TITLE: Time-Resolved Spectral Optical Breast Tomography

PRINCIPAL INVESTIGATOR: Min Xu
Melvin Lax, Ph.D.

CONTRACTING ORGANIZATION: The City College of the City
University of New York & The Research
Foundation of the City University of
New York
New York, NY 10031

REPORT DATE: June 2004

TYPE OF REPORT: Annual Summary

PREPARED FOR: U.S. Army Medical Research and Materiel Command
Fort Detrick, Maryland 21702-5012

DISTRIBUTION STATEMENT: Approved for Public Release;
Distribution Unlimited

The views, opinions and/or findings contained in this report are
those of the author(s) and should not be construed as an official
Department of the Army position, policy or decision unless so
designated by other documentation.

20041101 070

REPORT DOCUMENTATION PAGE

Public reporting burden for this collection of information is estimated to average 1 hour per response, including the time for reviewing instructions, searching existing data sources, gathering and maintaining the data needed, and completing and reviewing this collection of information. Send comments regarding this burden estimate or any other aspect of this collection of information, including suggestions for reducing this burden to Washington Headquarters Services, Directorate for Information Operations and Reports, 1215 Jefferson Davis Highway, Suite 1204, Arlington, VA 22202-4302, and to the Office of Management and Budget, Paperwork Reduction Project (0704-0188), Washington, DC 20503

1. AGENCY USE ONLY (Leave blank)	2. REPORT DATE June 2004	3. REPORT TYPE AND DATES COVERED Annual Summary (15 May 2003 – 15 May 2004)

4. TITLE AND SUBTITLE

Time-Resolved Spectral Optical Breast Tomography

5. FUNDING NUMBERS
DAMD17-02-1-0516

6. AUTHOR(S)

Min Xu
Melvin Lax, Ph.D.

7. PERFORMING ORGANIZATION NAME(S) AND ADDRESS(ES)
The City College of the City University of New York
& The Research Foundation of the City University of New York
New York, NY 10031
E-Mail: minxu@sci.ccny.cuny.edu

8. PERFORMING ORGANIZATION REPORT NUMBER

9. SPONSORING / MONITORING AGENCY NAME(S) AND ADDRESS(ES)

U.S. Army Medical Research and Materiel Command
Fort Detrick, Maryland 21702-5012

10. SPONSORING / MONITORING AGENCY REPORT NUMBER

11. SUPPLEMENTARY NOTES

12a. DISTRIBUTION / AVAILABILITY STATEMENT
Approved for Public Release; Distribution Unlimited

12b. DISTRIBUTION CODE

13. ABSTRACT (Maximum 200 Words)

The research carried out during the current reporting period involved: (a) developing and enhancing the 3D tomographic image reconstruction algorithm to use a L-curve method guided by the signal-to-noise ratio of the dataset to determine the regularization parameter; (b) developing and enhancing the 3D tomographic image reconstruction algorithm to make use of spectral information in multiple wavelength measurements; (c) developing a novel information theory approach to analyze the dataset for image reconstruction; and (d) extending the range of applicability of the linear inversion scheme for optical imaging using a nonlinear correction factor for inhomogeneities strong in absorption. The L-curve method guided by the signal-to-noise ratio of the dataset and the information theory approach using independent component analysis to analyze the dataset were found to improve the quality of image reconstruction. The correction for the nonlinear effect of the multiple passages of an absorption site by light was shown to be essential in optical imaging to characterize properly inhomogeneities strong in absorption. The theoretical formalism and computer algorithm for 3D tomographic image reconstruction shows with simulated data and preliminary experimental data the potential to provide fast 3D images of the scattering and absorption objects at various depths in turbid media.

14. SUBJECT TERMS
Medical and biological imaging; Optical mammography; Time-resolved Imaging; Image reconstruction techniques; spectroscopic imaging

15. NUMBER OF PAGES
38

16. PRICE CODE

17. SECURITY CLASSIFICATION OF REPORT Unclassified	18. SECURITY CLASSIFICATION OF THIS PAGE Unclassified	19. SECURITY CLASSIFICATION OF ABSTRACT Unclassified	20. LIMITATION OF ABSTRACT Unlimited

NSN 7540-01-280-5500

Table of Contents

Introduction

The "Time-resolved Spectral Optical Breast Tomography" research project aims to develop a near real-time three-dimensional (3D) spectral tomographic imaging algorithm with use of the cumulant approximation to radiative transfer to model light propagation in tissues. This project in this reporting period involves theoretical modeling of photon migration in tissues and image reconstruction, and working with the experimental group to apply and test the image reconstruction algorithm using experimental data obtained from phantoms. Significant advances were made during the current reporting period.

Body

The tasks performed and the progress made during the current reporting period include theoretical modeling of photon migration in tissues and image reconstruction, and working with the experimental group to apply and test the image reconstruction algorithm using experimental data obtained from phantoms.

Theoretical modeling of photon migration in tissue and image reconstruction

We continued to enhance the 3D tomographic image reconstruction algorithm based on the new cumulant transport model[1] to make use of spectral information when observations of multiple wavelengths are available (Task 1.3). By scanning a point source on the grids of the input plane of a slab and measuring light intensities on a detector array on the exit plane of the slab, a set of four-dimensional (4D) data is formed.[2, Appendix 1] The spectral information adds an additional dimension of the data. We started to investigate the optimal approach to analyze this huge dataset (Task 1.5). Some preliminary results were obtained from the application of information theory to the simulated and experimental dataset using Independent Component Analysis (ICA).[3, 4, Appendix 4] Improvement in the quality of image reconstruction was observed.

We improved the 3D tomographic image reconstruction algorithm to use a L-curve method guided by the signal-to-noise ratio of the dataset to determine the regularization parameter (Task 1.4).

We also studied the nonlinear effect of the multiple passages of light through an absorption inhomogeneity for optical imaging (Task 1). We derived the nonlinear correction factor (NCF) using the cumulant solution to radiative transfer. NCF was verified and supported by both Monte Carlo simulations and experiments. The nonlinear correction using NCF was shown to correct the underestimation of absorption by the conventional linear perturbation scheme of optical imaging when the inhomogeneity is strong in absorption.[5, 6, Appendix 3,5]

Apply and test the image reconstruction algorithm using experimental data

We worked with the experimental group at the Institute of Ultrafast Spectroscopy and Lasers at the City College of New York. The image reconstruction algorithm was modified to accept the data from the experimental group (Task 2). Experiments were performed to image objects inside tissue-like Intralipid-10% suspensions in water. Experimental results were analyzed and images were reconstructed using the 3D tomographic image reconstruction algorithm (Task 2.2).[3, 4, Appendix 4] We are working to fine tune the algorithm using the experimental data.

Further experiments will be performed on breast phantoms. Experiments to use multiple wavelengths and different configurations (transmission and backscattering) of the setup will be used to test and improve the 3D tomographic image reconstruction algorithm.

4

Key Research Accomplishments

- Developed and enhanced the 3D tomographic image reconstruction algorithm to use a L-curve method guided by the signal-to-noise ratio of the dataset to determine the regularization parameter.
- Developed and enhanced the 3D tomographic image reconstruction algorithm to make use of spectral information in multiple wavelength measurements.
- Developed a novel information theory approach to analyze the dataset for image reconstruction.
- Extended the range of applicability of the linear inversion scheme for optical imaging using a nonlinear correction factor for inhomogeneities strong in absorption

Reportable Outcomes

Journal Papers:

1. Cai, W., M. Xu, and R.R. Alfano, *Three dimensional radiative transfer tomography for turbid media.* IEEE JSTQE, 2003. **9**: p. 189-198. (Appendix 1)
2. Xu, M. and R.R. Alfano, *More on patterns in Mie scattering.* Opt. Comm., 2003. **226**(1-6): p. 1-5. (Appendix 2)
3. Xu, M., *Light extinction and absorption by arbitrarily oriented finite circular cylinders using geometrical path statistics of rays.* App. Opt., 2003. **42**: p. 6710-6723
4. Xu, M., W. Cai, and R.R. Alfano, *Multiple passages of light through an absorption inhomogeneity in optical imaging of turbid media.* Opt. Lett., 2004 (in press) (Appendix 5)

Presentations and Proceeding Papers:

5. Xu, M., W. Cai, and R.R. Alfano. *Nonlinear multiple passage effects on optical imaging of an absorption inhomogeneity in turbid media.* in *European Conference on Biomedical Optics: Photon migration and Diffuse-light imaging.* 2003.(Appendix 3)
6. Xu, M., et al., *Simulated and experimental separation and characterization of absorptive inhomogeneities embedded in turbid media,* in *Biomedical topical meetings on cd-rom (osa).* 2004: Fontainebleau Hilton Resort and Towers, Miami Beach, Florida. WF25 (Appendix 4).
7. Al-rubaiee, M., et al., *Time-resolved and quasi-continuous wave three-dimensional tomographic imaging,* in *Femtosecond laser applications in biology.* 2004: Palais de la Musique et des Congrès de Strasbourg, Strasbourg, France.

Grant application:

Applied for breast cancer concept award "Localization and Identification of Tumor for Optical Breast Imaging" for BC03-CA.

Conclusions

The work carried out during the current reporting period builds on and affirms some of our earlier inferences and leads to the following conclusions. *First,* the L-curve method guided by the signal-to-noise ratio of the dataset and the information theory approach using independent component analysis to analyze the dataset were found to improve the quality of image reconstruction. *Second,* the 3D tomographic image reconstruction algorithm was enhanced to make use of spectral information in multiple wavelength measurements; *Third,* the correction for the nonlinear effect of the multiple passages of an absorption site by light was shown to be essential in optical imaging to characterize properly inhomogeneities strong in absorption. *Fourth,* the theoretical formalism and computer algorithm for 3D tomographic image

reconstruction shows (with simulated and experimental data) the potential to provide fast 3D images of the scattering and absorption objects at various depths in turbid media.

References

1. Xu, M., et al., *Photon migration in turbid media using a cumulant approximation to radiative transfer.* Phys. Rev. E, 2002. **65**: p. 066609.
2. Cai, W., M. Xu, and R.R. Alfano, *Three dimensional radiative transfer tomography for turbid media.* IEEE JSTQE, 2003. **9**: p. 189-198.
3. Xu, M., et al., *Simulated and experimental separation and characterization of absorptive inhomogeneities embedded in turbid media,* in *Biomedical topical meetings on cd-rom (osa).* 2004: Fontainebleau Hilton Resort and Towers, Miami Beach, Florida. p. WF25.
4. Al-rubaiee, M., et al., *Time-resolved and quasi-continuous wave three-dimensional tomographic imaging,* in *Femtosecond laser applications in biology.* 2004: Palais de la Musique et des Congrès de Strasbourg, Strasbourg, France.
5. Xu, M., W. Cai, and R.R. Alfano, *Multiple passages of light through an absorption inhomogeneity in optical imaging of turbid media.* Opt. Lett., 2004.
6. Xu, M., W. Cai, and R.R. Alfano. *Nonlinear multiple passage effects on optical imaging of an absorption inhomogeneity in turbid media.* in *European Conference on Biomedical Optics: Photon migration and Diffuse-light imaging.* 2003.

Three-Dimensional Radiative Transfer Tomography for Turbid Media

W. Cai, M. Xu, and R. R. Alfano

Abstract—The photon distribution, as a function of position, angle, and time, is computed using the analytical cumulant solution of the Boltzmann radiative transfer equation (RTE). A linear forward model for light propagation in turbid media for three-dimensional (3-D) optical tomography is formed based on this solution. The model can be used with time resolved, continuous wave (CW), and frequency-domain measurements in parallel geometries. This cumulant forward model (CFM) is more accurate than that based on the diffusion approximation of RTE. An inverse algorithm that incorporates this CFM is developed, based on a fast 3-D hybrid-dual-Fourier tomographic approach using multiple detectors and multiple sources in parallel geometries. The inverse algorithm can produce a 3-D image of a turbid medium with more than 20 000 voxels in 1–2 min using a personal computer. A 3-D image reconstructed from simulated data is presented.

Index Terms—Absorption and scattering, forward model, inverse algorithm, optical tomography, photon migration, radiative transfer equation (RTE).

I. INTRODUCTION

OVER THE PAST decade, optical tomography has been investigated as a noninvasive imaging method that uses nonionizing near-infrared (NIR) light to obtain images of the interior of the breast. Unlike X-ray, which is attenuated through media by ionizing the electrons at inner-orbits of atoms, NIR light uses the vibrational overtones for different molecular components in the structures of tumor. NIR light may be used to create image based on the molecular change, which may be used to improve sensitivity and specificity in the early diagnostics of breast cancer. Breast tissues scatter light strongly, and blur the direct shadow image of a tumor. A technique, known as inverse image reconstruction, has been investigated to overcome the problem of multiple scattering. Some obstacles in the development of optical tomography are inaccuracy of the commonly used diffusion forward model, and lack of a fast inverse algorithm able to realize a three-dimensional (3-D) image reconstruction of a breast for clinical use.

One critical issue is the forward model, which should correctly simulate photon propagation in the medium. The most commonly used forward models were built based on solution

of the diffusion equation, which is the lowest approximation of the radiative transfer equation (RTE) [1]–[5]. The forward models based on the diffusion approximation (DA) give a large error when the distance d between a voxel and a source is small. Furthermore, the photon distribution still maintains a strong anisotropy in a deeper region away from a source, which will be shown later in this paper. Unfortunately, contributions from near surface voxels to measured signals are often larger than contributions from the voxels deep inside the medium. Inaccuracy of the DA-based forward model may lead to a failure in image reconstruction, especially for small hidden objects deep inside the medium. The total weight matrix should be inverted. The large elements in the matrix, which play a more important role in inversion, are evaluated incorrectly in DA models. The shortcoming of DA is well recognized, but it is still broadly applied due to the difficulty in directly solving the radiative transfer equation. Hielscher *et al.* [6] and Vihunen *et al.* [7] developed numerical solutions of RTE for optical tomography.

Recently, we have developed an analytical solution of RTE, based on cumulant expansion, in an infinite uniform medium with an arbitrary phase function [8], [9]. It provides an explicit analytical expression for photon distribution function $I(\mathbf{r}, \mathbf{s}, t)$, as a function of position $\mathbf{r}$, direction of light $\mathbf{s}$, and time t. The mean position and the half-width at half-maximum (HWHM) height of the distribution are always exact. In this paper, the linear forward model based on the cumulant solution is described. This CFM may used with time-resolved, continuous wave (CW), and frequency-domain data, which are much more accurate than the DA models.

To obtain a 3-D image one needs to investigate the inverse algorithms. For clinical applications, this requires an inversion technique, that is computationally fast, and stable in the presence of measurement noise. Recent algorithms to solve the inverse problem include Newton's least-square-based methods and gradient-descent methods [1]–[5]. These approaches use an iterative procedure, which requires a long computation time to solve a 3-D inverse problem with large unknowns (the number of unknowns is the number of voxels). Furthermore, the iterative methods can not ensure that the result arrives at a "global minimum," and does not converge to a "local minimum," which is not a true image of the medium. The application of Fourier transform, which has been called "diffraction tomography," can greatly reduce computation time. Matson *et al.* [10] and Li *et al.* [11] have developed the diffraction optical tomographic methods to realize fast image reconstruction. However, their algorithms are limited to the use of a single light source with a two-dimensional (2-D) plane

of detectors. This type of experimental setup acquires only a set of 2-D data using CW or frequency-modulated light, that is not enough for a 3-D image reconstruction. Recently, Schotland and Markel developed inverse inversion algorithms using diffusion tomography [12]–[14] based on the analytical form of the Green's function of frequency-domain diffusive waves, and point-like absorbers and scatterers. Data obtained by multiple sources with multiple detectors in parallel slab geometry are used in these approaches.

A fast hybrid-dual-Fourier (HDF) algorithm, which uses multiple sources and multiple detectors in parallel slab geometry, is described in this paper for reconstruction of a 3-D image of an inhomogeneous medium. This approach uses a general 2-D translation invariance of the Green's function in a homogeneous background slab medium, suitable for forward models based on solution of RTE, and various other forward models, in CW, frequency-domain, and time-resolved measurements. This inverse algorithm runs fast. It is shown that a 3-D image of a turbid medium (for example, divided into $32 \times 32 \times 20 = 20\,480$ voxels) can be reconstructed in 1–2 min using a personal computer. This algorithm can produce stable images in presence of relatively strong noises.

The forward model and the inverse algorithm discussed in the following can also be applied for image reconstruction in a cloudy environment for military use.

This paper is organized as follows. Section II presents the analytical solution of RTE, based on a cumulant expansion, in an infinite uniform medium and shows the photon distribution function computed using the cumulant analytical solution. Section III describes the forward models based on the analytical solution of RTE, considering the slab geometry, and a weak heterogeneity using a perturbative method. Section IV describes the HDF inverse algorithm for a reconstruction of a 3-D image of an inhomogeneous medium. The 3-D image using this algorithm is shown. A discussion is presented in Section V.

II. ANALYTICAL CUMULANT SOLUTION OF RTE

The photon propagation in a medium is described by the photon distribution function, $I(\mathbf{r}, \mathbf{s}, t)$, as a function of time t, position $\mathbf{r}$, and direction $\mathbf{s}$. The mathematical equation governing photon propagation is the well-known radiative transfer equation

$$\partial I(\mathbf{r}, \mathbf{s}, t)/\partial t + c\mathbf{s} \cdot \nabla_r I(\mathbf{r}, \mathbf{s}, t) + \mu_a(\mathbf{r}) I(\mathbf{r}, \mathbf{s}, t)$$
$$= \mu_s(\mathbf{r}) \int P(\mathbf{s}, \mathbf{s}', \mathbf{r})[I(\mathbf{r}, \mathbf{s}', t) - I(\mathbf{r}, \mathbf{s}, t)]\, ds'$$
$$+ \delta(\mathbf{r} - \mathbf{r}_0)\delta(\mathbf{s} - \mathbf{s}_0)\delta(t - 0) \qquad (1)$$

where the fundamental parameters are the scattering rate $\mu_s(\mathbf{r}) = c\rho\sigma_s$, the absorption rate $\mu_a(\mathbf{r}) = c\rho\sigma_a$, and the differential angular scattering rate $\mu_s(\mathbf{r}) P(\mathbf{s}, \mathbf{s}', \mathbf{r})$, where σ_a and σ_s are the absorption and scattering cross sections respectively, ρ is density of scatterers, and c is the speed of light in the medium. In a uniform infinite medium, these parameters are position independent.

When the phase function depends only on the scattering angle, we can expand the phase function in Legendre polynomials with constant coefficients

$$P(\mathbf{s}, \mathbf{s}') = \frac{1}{4\pi} \sum_l a_l P_l[\cos(\mathbf{s} \cdot \mathbf{s}')]. \qquad (2)$$

Recently, we have developed a new approach to obtain an analytical solution of RTE, based on a cumulant expansion, in an infinite uniform medium, with an arbitrary phase function $P(\mathbf{s}, \mathbf{s}')$ [8], [9].

We briefly review the concept of "cumulant" in a one-dimensional (1-D) case. Consider a random variable x, with a probability distribution function $f(x)$. Instead of using $f(x)$ to describe the distribution, we define the nth moment of x, $\langle x^n \rangle = \int x^n f(x)\, dx$, and correspondingly the nth cumulant $\langle x^n \rangle_c$ defined by $\exp(\sum_{n=1}^{\infty} \langle x^n \rangle_c (it)^n/n!) = \langle \exp(itx) \rangle = \sum_{n=0}^{\infty} \langle x^n \rangle (it)^n/n!$. The first cumulant $\langle x \rangle_c$ is the mean position of x. The second cumulant $\langle x^2 \rangle_c$ represents the HWHM of the distribution. The higher cumulants are related to the detailed shape of the distribution. For example, $\langle x^3 \rangle_c$ describes the skewness or asymmetry of the distribution, and $\langle x^4 \rangle_c$ describes the "kurtosis" of the distribution, that is the extent to which it differs from the standard bell shape associated with the normal distribution function. The cumulants, hence, describe the distribution in an intrinsic way by subtracting off the effects of all lower order moments. In 3-D case, the first cumulant has three components, the second cumulant has six components, and so on.

We derived an explicit algebraic expression of spatial cumulants at any angle and any time that is exact up to an arbitrarily high order n [9]. This means the distribution function $I(\mathbf{r}, \mathbf{s}, t)$ can be computed to any desired accuracy. At the second order, $n = 2$, an analytic, hence, useful explicit expression for distribution function $I(\mathbf{r}, \mathbf{s}, t)$ is obtained [8]. This distribution is Gaussian in position, which is accurate at later times, but only provides the exact mean position and the exact HWHM at early times. A weakness of the second order cumulant solution is that photons at the front edge of Gaussian distribution travel faster than light speed, thus violate causality, though to a much less extent than that in the DA.

Fig. 1 compares $I(\mathbf{r}, \mathbf{s}, t)$ obtained from the analytical cumulant solution and the Monte Carlo (MC) simulation. In order to reduce the statistical deviation to an acceptable level, 10^9 events are counted in the MC simulation. The figure shows that the solid curve (the tenth-order cumulant solution) is located in the middle of data obtained by the MC simulation. The solution for CW case can be obtained by an integration of $I(\mathbf{r}, \mathbf{s}, t)$ over time t. It is shown that even second order cumulant solution (the dotted curve) can provide an accurate CW solution, because this solution ensures that the mean position and the HWHM of distribution are always exact.

The plots in Fig. 1 indicate that a strong anisotropic angular distribution still exists at $z \sim 6\,l_{tr}$ (l_{tr} is the transport mean free path) from the source. The DA is only valid when the angular distribution is nearly isotropic. The dominate s wave distribution $N(\mathbf{r}, t)/4\pi$ computed using the diffusion model (the thick dotted curve) has a large discrepancy with the MC result.
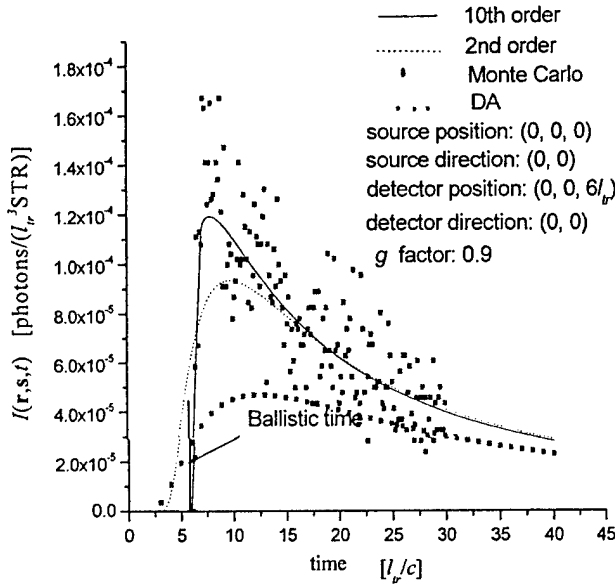
Fig. 1. Distribution function $I(\mathbf{r}, \mathbf{s}, t)$ in an infinite uniform scattering medium as a function of time t, using Henyey–Greenstein phase function with $g = 0.9$. The detector is located at $R = 6\, l_{tr} = 60\, l_s$ from the source front along direction of incident light, and the direction is along the incident direction. The solid curve is computed from approximation up to tenth order of cumulant; the dotted curve is computed from approximation up to the second order of cumulant, the discrete dots are from the MC simulation; the curve of thick dots is from the DA, $N(\mathbf{r}, t)/4\pi$.

The second-order analytical cumulant solution is given by [8]

$$I(\mathbf{r}, \mathbf{s}, t) = \frac{F(\mathbf{s}, \mathbf{s}_0, t)}{(4\pi)^{3/2}} \frac{1}{(\det B)^{1/2}}$$

$$\cdot \exp\left[-\frac{1}{4}(B^{-1})_{\alpha\beta}(r - r^c)_\alpha(r - r^c)_\beta\right] \quad (3)$$

where

$$F(\mathbf{s}, \mathbf{s}_0, t)$$
$$= \exp(-\mu_a t) \sum_l \frac{2l + 1}{4\pi} \exp(-g_l t) P_l[\cos(\mathbf{s} \cdot \mathbf{s}_0)]$$
$$= \exp(-\mu_a t) \sum_l \frac{2l + 1}{4\pi} \exp(-g_l t) \sum_m Y_{lm}(\mathbf{s}) Y_{lm}^*(\mathbf{s}_0).$$

$$(4)$$

In (4), $g_l = \mu_s[1 - a_l/(2l + 1)]$, $Y_{lm}(\theta, \phi) = (-1)^m[(l - m)!/(l + m)!]^{1/2} P_l^{(m)}(\cos\theta) \exp(im\phi)$, where $P_l^{(m)}(\cos\theta)$ is the associated Legendre function, and $Y_{lm}(\mathbf{s})$ are spherical harmonics normalized to $4\pi/(2l + 1)$.

In (3), the mean position of the distribution (first cumulant), when the source is located at $\mathbf{r}_0 = 0$ and the incident direction is along z, is given by

$$r_z^c(\mathbf{s}, t) = G \sum_l A_l P_l(\cos\theta)$$
$$\cdot [(l + 1)f(g_l - g_{l+1}) + lf(g_l - g_{l-1})] \quad (5.1)$$

$$r_x^c(\mathbf{s}, t) = G \sum_l A_l P_l^{(1)}(\cos\theta)$$
$$\cdot \cos\phi[f(g_l - g_{l-1}) - f(g_l - g_{l+1})] \quad (5.2)$$

where

$$G = c\exp(-\mu_a t)/F(\mathbf{s}, \mathbf{s}_0, t)$$
$$f(g) = [\exp(gt) - 1]/g$$
$$A_l = (1/4\pi)\exp(-g_l t) \quad (6)$$

r_y^c is obtained by replacing $\cos\phi$ in (5.2) by $\sin\phi$.

The HWHM (second cumulant) is expressed as

$$B_{\alpha\beta}(\mathbf{s}, t) = cG\Delta_{\alpha\beta} - r_\alpha^c r_\beta^c/2 \quad (7)$$

with

$$\Delta_{zz} = \sum_l A_l P_l(\cos\theta)\left[\frac{l(l-1)}{2l-1}E_l^{(1)} + \frac{(l+1)(l+2)}{2l+3}E_l^{(2)}\right.$$
$$\left. + \frac{l^2}{2l-1}E_l^{(3)} + \frac{(l+1)^2}{2l+3}E_l^{(4)}\right] \quad (8.1)$$

$$\Delta_{xx,yy} = \sum_l \frac{1}{2}A_l P_l(\cos\theta)\left[-\frac{l(l-1)}{2l-1}E_l^{(1)}\right.$$
$$\left. -\frac{(l+1)(l+2)}{2l+3}E_l^{(2)} + \frac{l(l-1)}{2l-1}E_l^{(3)}\right.$$
$$\left. + \frac{(l+1)(l+2)}{2l+3}E_l^{(4)}\right] \pm \sum_l \frac{1}{2}A_l P_l^{(2)}(\cos\theta)$$
$$\cdot \cos(2\phi)\left[\frac{1}{2l-1}E_l^{(1)} + \frac{1}{2l+3}E_l^{(2)}\right.$$
$$\left. -\frac{1}{2l-1}E_l^{(3)} - \frac{1}{2l+3}E_l^{(4)}\right] \quad (8.2)$$

where $(+)$ corresponds to Δ_{xx} and $(-)$ corresponds to Δ_{yy}.

$$\Delta_{xy} = \sum_l \frac{1}{2}A_l P_l^{(2)}(\cos\theta)\sin(2\phi)\left[\frac{1}{2l-1}E_l^{(1)}\right.$$
$$\left. + \frac{1}{2l+3}E_l^{(2)} - \frac{1}{2l-1}E_l^{(3)} - \frac{1}{2l+3}E_l^{(4)}\right] \quad (8.3)$$

$$\Delta_{xz} = \sum_l \frac{1}{2}A_l P_l^{(1)}(\cos\theta)\cos(\phi)\left[\frac{2(l-1)}{2l-1}E_l^{(1)}\right.$$
$$\left. -\frac{2(l+2)}{2l+3}E_l^{(2)} + \frac{1}{2l-1}E_l^{(3)} + \frac{1}{2l+3}E_l^{(4)}\right].$$
$$(8.4)$$

Δ_{yz} is obtained by replacing $\cos\phi$ in (8.4) by $\sin\phi$. In (8.1)–(8.4) $E_l^{(1-4)}$ are given by

$$E_l^{(1)} = [f(g_l - g_{l-2}) - f(g_l - g_{l-1})]/(g_{l-1} - g_{l-2}) \quad (9.1)$$

$$E_l^{(2)} = [f(g_l - g_{l+2}) - f(g_l - g_{l+1})]/(g_{l+1} - g_{l+2}) \quad (9.2)$$

$$E_l^{(3)} = [f(g_l - g_{l-1}) - t]/(g_l - g_{l-1}) \quad (9.3)$$

$$E_l^{(4)} = [f(g_l - g_{l+1}) - t]/(g_l - g_{l+1}). \quad (9.4)$$

Fig. 2(a) and (b) shows the light distribution as a function of time at different receiving angles in an infinite uniform medium, computed by the second cumulant solution, where detector is located, separately, at $5\, l_{tr}$ [Fig. 2(a)] and $15\, l_{tr}$ [Fig. 2(b)] from the source in the incident direction of the source. Fig. 2 shows the existence of the strong anisotropy of the light distribution at
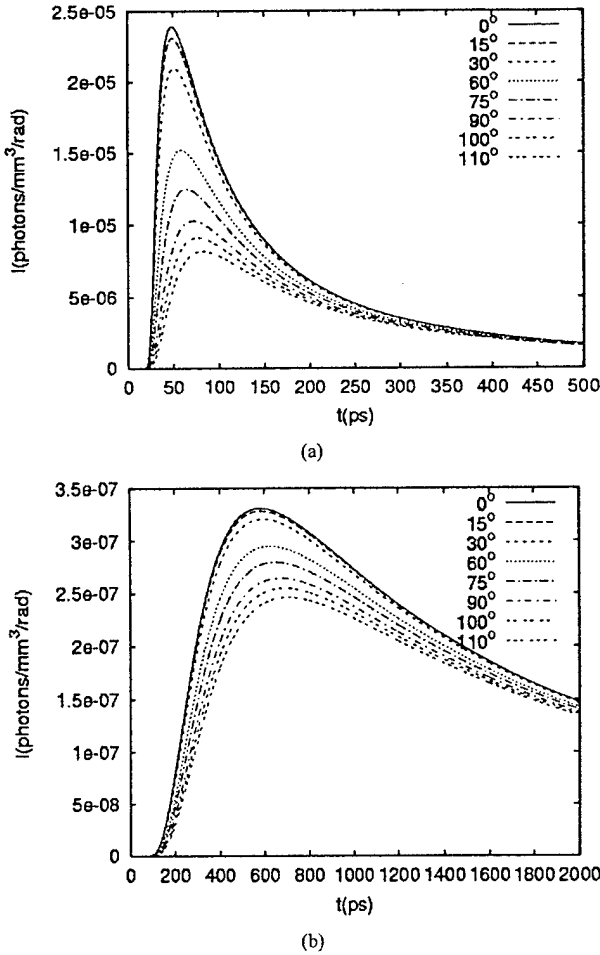
(a)

(b)

Fig. 2. Light distribution in an infinite uniform medium as a function of time at different received angle, using second cumulant solution of radiative transfer equation, where detector is located, separately, at 10 [Fig. 2(a)] and 30 mm [Fig. 2(b)] from the source in the incident direction. The parameters for this calculation are: $l_{tr} = 2$ mm, $l_a = 300$ mm, the phase function is computed using Mie theory for polystyrene spheres with diameter $d = 1.11$ μm in water and the wavelength of laser source $\lambda = 625$ nm, which gives the g-factor $g = 0.926$.

5 l_{tr} from the source and the modest anisotropy at a distance of 15 l_{tr}. These types of distributions have been demonstrated by time-resolved experiments [15].

One advantage of using the above analytical solution of RTE is that the distribution function can be computed very fast. The associated Legendre functions can be accurately computed using recurrence relations. It takes only a minute to compute 10^5 data of $I(\mathbf{r}, \mathbf{s}, t)$ on a personal computer.

The corresponding solution in the frequency-domain $I(\mathbf{r}, \mathbf{s}, \omega)$ can be obtained by making a Fourier transform $\int dt \exp(-i\omega t) I(\mathbf{r}, \mathbf{s}, t)$. The CW solution is obtained by taking $\omega = 0$.

The photon density $N(\mathbf{r}, t)$ of the second cumulant solution is given by

$$N(\mathbf{r}, t) = \frac{1}{(4\pi D_{zz}ct)^{1/2}} \frac{1}{4\pi D_{xx}ct} \exp\left[-\frac{(z - R_z)^2}{4D_{zz}ct}\right]$$
$$\cdot \exp\left[-\frac{(x^2 + y^2)}{4D_{xx}ct}\right] \exp(-\mu_a t) \quad (10)$$

with the mean position

$$R_z = c[1 - \exp(-g_1 t)]/g_1. \quad (11)$$

The corresponding time-dependent diffusion coefficients are

$$D_{zz} = \frac{c}{3t}\left\{\frac{t}{g_1} - \frac{3g_1 - g_2}{g_1^2(g_1 - g_2)}[1 - \exp(-g_1 t)]\right.$$
$$+ \frac{2}{g_2(g_1 - g_2)}[1 - \exp(-g_2 t)]$$
$$\left. - \frac{3}{2g_1^2}[1 - \exp(-g_1 t)]^2\right\} \quad (12)$$

$$D_{xx} = D_{yy}$$
$$= \frac{c}{3t}\left\{\frac{t}{g_1} + \frac{g_2}{g_1^2(g_1 - g_2)}[1 - \exp(-g_1 t)]\right.$$
$$\left. - \frac{1}{g_2(g_1 - g_2)}[1 - \exp(-g_2 t)]\right\}. \quad (13)$$

As shown in (11)–(13), the mean position of the distribution is moving, and the diffusion coefficients are time dependent. At $t \rightarrow 0$, the mean position of the photon density moves along z direction with speed c, and the diffusion coefficients tend to zero, this result presents a clear picture of near ballistic motion. As time increases, the mean position motion slows down, and the diffusion coefficients increase from zero. This stage of photon migration is often called a snakelike mode. At long time, (10) tends to the center-moved (1 l_{tr}) diffusion model with the diffusion coefficient $l_{tr}/3$.

III. FORWARD MODEL BASED ON THE CUMULANT SOLUTION OF RTE

The linear forward models for scattering media are built in following three steps: 1) computation of a background Green's function in an infinite uniform medium; 2) extension of this Green's function to slab geometry; and 3) computation of the weight function using a perturbative method. These steps have been applied in building the linear forward models under DA [2]. We use these steps as well, but our approach is based on the cumulant solution of RTE, rather than the solution of the diffusion equation.

We use the second-order cumulant solution for computing a background Green's function in an infinite uniform medium, since it is easy to use the explicit expressions in (3)–(9), that avoid complicated computations of higher order cumulants. The second order cumulant solution is accurate at later times, but only provides the correct mean position and the correct HWHM at early times. We notice that the width of the distribution at early times could be smaller than the size of a voxel, the average over the distributions at different points in a voxel smears the detail shape of the distribution. In the CW or frequency- domain cases, the shape of the distribution is further smeared by integration over time t. Therefore, the second-order cumulant solution can be a reasonable approximation in building forward models based on the RTE.

Since a detector usually collects emergent light within a wide range of angle of different directions, it is convenient to compute the Green's function related to a detector using photon density $N(\mathbf{r}_d, t)$ (10)–(13), where $\mathbf{r}_d$ is the position of detector.
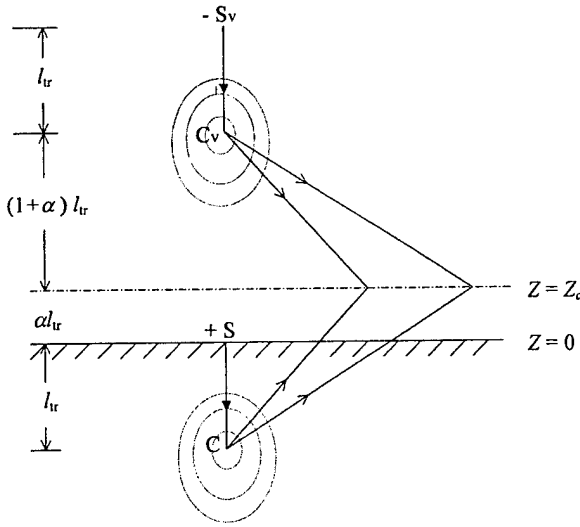
Fig. 3. Schematic diagram shows how to extend the cumulant solution of RTE from an infinite medium to a semi-infinite medium.

Fig. 4. Backscattered photon distribution $I(\mathbf{r}, \mathbf{s} = -\mathbf{z}, t)$ emerging from plane surface of a semi-infinite turbid medium, as a function of time, with the source-detector distance $1\ l_{tr}$ on the surface $z = 0$ plane. The pulse source is located at $z = 0$, incident along z direction. The extrapolated boundary condition is used. The solid curve is obtained from cumulant approximation (CA), up to the second cumulant. The dashed curve is from DA. The cross points are obtained from MC simulation.

It is essential to include the boundary effect in the solution of the RTE when photons are injected into and spread out from a finite sized medium. A proper extension of the cumulant solution to slab geometry is an essential step for building a forward model.

A boundary condition is applied based on the following physical consideration. At early times, the center of photon distribution injected into medium, moves forward into medium. Then, the distribution spreads out from the moving center with diffusion coefficients that gradually increase from zero. At early times, the number of photons leaking out of the boundary is negligible compared to the total number of the incident photons. The boundary condition plays a role at later times, when there are many photons leaking out of the boundary.

The approach known as an approximate "extrapolated" boundary condition [16], extrapolates the boundary by a distance $\xi = \alpha l_{tr}$, the extrapolation length, beyond the real boundaries with $\alpha \sim 0.7$, at which the photon density vanishes.

To apply this boundary condition for the cumulant solution in a semi-infinite geometry a, a virtual negative source S_v is added to the original source S, as shown in Fig. 3. During the early period, the solution of the RTE in an infinite uniform medium automatically satisfied the boundary condition because the density is near zero at the boundary, and the virtual source does not play a role. After a time of approximately $4\ l_{tr}/c$, the center of photon density, C, has moved and stopped at a position $1\ l_{tr}$ from the original source S and the center from virtual source, C_v, has moved in a similar way. Then, the arrangement shown in Fig. 3, produces a cancellation of contributions to the photon density from the original source and the virtual source on the extrapolated boundary.

Fig. 4 shows that the time-resolved backscattered photon distribution in a semi-infinite medium on the $z = 0$ surface, with the source-detector distance $1\ l_{tr}$, obtained using the seco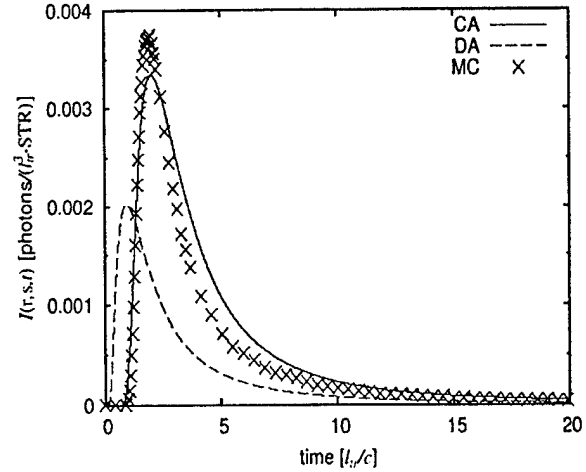nd-order cumulant approximation and the extrapolated boundary condition, which agrees with the MC simulation much better than that of the DA.

For extending to the slab geometry, adding a series of pairs of virtual "image" sources at both sides of slab is a good approximation for satisfaction of the extrapolated boundary conditions on both sides of a slab [17].

The heterogeneous structure of a highly scattering turbid medium can be characterized by the following optical parameters: the scattering rate $\mu_s(\mathbf{r})$, the absorption rate $\mu_a(\mathbf{r})$, and the differential angular scattering rate $\mu_s(\mathbf{r})P(\mathbf{s}, \mathbf{s}', \mathbf{r})$.

A perturbation method is used which takes the photon distribution function in a uniform background slab medium as the zero-order approximation. The change of the photon distribution function originates from the change of optical parameters compared to that in the uniform background slab medium. The change of scattering and absorption parameters are defined as follows:

$$\Delta\mu_s(\mathbf{r}) = \mu_s(\mathbf{r}) - \mu_s^{(0)}$$

$$\Delta\mu_a(\mathbf{r}) = \mu_a(\mathbf{r}) - \mu_a^{(0)}$$

$$\Delta[\mu_s P](\mathbf{s}, \mathbf{s}', \mathbf{r}) = \mu_s(\mathbf{r})P(\mathbf{s}, \mathbf{s}', \mathbf{r}), -\mu_s^{(0)}P^{(0)}(\mathbf{s}, \mathbf{s}') \quad (14)$$

where the quantities with super index (0) are the optical parameters in a uniform background slab medium. By expanding $\Delta[\mu_s P]$ ($\mathbf{s}, \mathbf{s}', \mathbf{r}$) in Legendre polynomials, we obtain

$$\Delta[\mu_s P](\mathbf{s}, \mathbf{s}', \mathbf{r})$$
$$= \frac{1}{4\pi}\sum_l [\Delta\mu_s(\mathbf{r})a_l^{(0)} + \mu_s^{(0)}\Delta a_l(\mathbf{r})]P_l[\cos(\mathbf{s}\cdot\mathbf{s}')] \quad (15)$$

with $\Delta a_0(\mathbf{r}) = 0$, since a_0 always equals 1. The physical meaning is that the scattering parameters have no effect on the s $(l = 0)$ component.

Making a perturbation expansion of (1) to the first-order Born approximation, the change in the photon distribution is given by

$$
\Delta I(r_d, s_d, t \mid r_s, s_s)
$$
$$
= \int dt' \int dr \int ds' I^{(0)}(r_d, s_d, t - t' \mid r, s')
$$
$$
\cdot \left\{ \int \Delta[\mu_s P](s, s', r) I^{(0)}(r, s, t' \mid r_s, s_s) \, ds \right.
$$
$$
\left. - [\Delta\mu_s(r) + \Delta\mu_a(r)] I^{(0)}(r, s', t' \mid r_s, s_s) \right\} \quad (16)
$$

where $\Delta I(r_d, s_d, t \mid r_s, s_s)$ is the change in the light intensity received by a detector located at r_d, along the direction s_d, and at time t, which is injected from a source located at r_s, along a direction of s_s, at time $t = 0$. "Change" refers to the difference in intensity compared to that received by the same detector, from the same source, when light passes through a uniform background slab medium. The term $I^{(0)}(r_2, s_2, t \mid r_1, s_1)$ is the intensity of light, calculated using the cumulant solution of RTE, at r_2 along the direction s_2 and at time t, when light is injected from a position r_1 along a direction of s_1 at time $t = 0$ migrating in a uniform background slab medium.

The background Green's functions in (16), obtained by cumulant solution, are expanded in spherical harmonics

$$
I^{(0)}(r, s, t' \mid r_s, s_s) = \sum_{l,m} A_{lm}(r, r_s, s_s, t') Y_{lm}(s),
$$
$$
I^{(0)}(r_d, s_d, t - t' \mid r, s) = \sum_{l,m} C^*_{lm}(r, r_d, s_d, t - t') Y^*_{lm}(s).
$$
$$
\quad (17)
$$

The spherical transform is performed using a fast Fourier transform for the integral over ϕ, and a Clenshaw–Curtis quadrature for the integral over θ.

Using the orthogonality relation of the spherical function and the addition theorem: $\sum_m Y_{lm}(s) Y^*_{lm}(s') = P_l[\cos(s \cdot s')]$, the analytical integration over s and s' in (16) can be performed. For time resolved data, the contribution from an absorbing object located at r_k is given by

$$
\Delta I(r_d, s_d, r_s, s_s, t \mid r_k)
$$
$$
= -\Delta\mu_a(r_k) \delta V_k \int_0^t dt' \sum_{l=0}^L \frac{4\pi}{(2l+1)}
$$
$$
\cdot \sum_m A_{lm}(r_k, r_s, s_s, t') C^*_{lm}(r_k, r_d, s_d, t - t') \quad (18)
$$

where δV_k is the volume of kth voxel, and L is the cutoff value in the Legendre expansion in (18). The contribution from a scattering object located at r_k is given by

$$
\Delta I(r_d, s_d, r_s, s_s, t \mid r_k)
$$
$$
= -\delta V_k \int_0^t dt' \sum_{l=1}^L \frac{4\pi}{(2l+1)}
$$
$$
\cdot \left[\Delta\mu_s(r_k) \left(1 - \frac{a_l^{(0)}}{2l+1}\right) - \mu_s^{(0)} \frac{\Delta a_l(r_k)}{2l+1} \right]
$$
$$
\cdot \sum_m A_{lm}(r_k, r_s, s_s, t') C^*_{lm}(r_k, r_d, s_d, t - t'). \quad (19)
$$

For frequency domain (or CW) data, the contribution from an absorbing object located at r_k is given by

$$
\Delta I(r_d, s_d, r_s, s_s, \omega \mid r_k)
$$
$$
= -\Delta\mu_a(r_k) \delta V_k \sum_{l=0}^L \frac{4\pi}{2l+1}
$$
$$
\cdot \sum_m A_{lm}(r_k, r_s, s_s, \omega) c^*_{lm}(r_k, r_d, s_d, \omega) \quad (20)
$$

and the contribution from a scattering object located at r_k is given by

$$
\Delta I(r_d, s_d, r_s, s_s, \omega \mid r_k)
$$
$$
= -\delta V_k \sum_{l=1}^L \frac{4\pi}{2l+1}
$$
$$
\cdot \left[\Delta\mu_s(r_k) \left(1 - \frac{a_l^{(0)}}{2l+1}\right) - \mu_s^{(0)} \frac{\Delta a_l(r_k)}{2l+1} \right]
$$
$$
\cdot \sum_m A_{lm}(r_k, r_s, s_s, \omega) c^*_{lm}(r_k, r_d, s_d, \omega). \quad (21)
$$

Comparing (18)–(21) with the corresponding weight function commonly used in the DA, [1], [2] only s wave ($l = 0$) for absorptive objects, and only p wave ($l = 1$) for scattering objects are considered in the diffusion forward models. Besides, even for s wave and p wave, the diffusive solution is incorrect when voxels are located near the source, as discussed before.

The previous formulae allow simulating the background Green's function and the change of optical parameters in detail. They are also applicable to the cases where only a few parameters of the medium are known, similar to that for the diffusion forward model. When only $\mu_s^{(0)}$, $\mu_a^{(0)}$, and g-factor for an uniform background medium are given, the Henyey–Greenstein phase function [18] is widely adopted as an approximate phase function

$$
P(\cos\theta) = \frac{1}{4\pi} \frac{1 - g^2}{(1 + g^2 - 2g\cos\theta)^{3/2}}
$$
$$
= \frac{1}{4\pi} \sum_l (2l + 1) g^l P_l(\cos\theta). \quad (22)
$$

Although (22) uses a single parameter g-factor to describe a phase function, this description is much better than that used in the DA, which implies a phase function linear in $\cos\theta$.

If $\Delta a_l(r)$ in (21), which represent the change of the phase function, is not considered, two optical parameters being imaged are $\Delta\mu_a(r)$ and $\Delta\mu_s(r)$. The reduced scattering coefficient $\Delta\mu_s(1 - a_1^{(0)}/3)$ is directly related to ΔD (change of the diffusion coefficient) used in the DA models. The CFM, hence, can be applied to the experimental data in a similar fashion as that for the DA models, to obtain images of the optical parameters. In the CFM, however, all contributions from higher spherical waves are properly included.

The most time consuming part in computation of CFM using the previous formulae is to build a database of A_{lm} and C^*_{lm}. Once it is built for a uniform background medium, the database can be applied for imaging of various heterogeneity cases. In parallel geometry, A_{lm} is a function of $(x_k - x_s, y_k - y_s)$ due to the 2-D translation invariance. Since position of source z_s and

incident direction s_s are fixed, only a 3-D $(x_k - x_s, y_k - y_s, z_k)$ database is required. When s_s is taken along z direction (light is injected perpendicular to surface), the scale of database is reduced to 2-D due to the z axis symmetry. Photons from different directions in a wide solid angle are received by a detector, as discussed before, photon density $N(r_d - r, s, t)$ is used for computing the Green's function associated with detectors, which is independent of s_d, and C_{lm}^* can be computed much easily. The database can be built in a reasonable computation time because the distribution function $I^{(0)}(r_2, s_2, t \mid r_1, s_1)$ can be rapidly calculated using the analytical expressions.

IV. FAST 3-D HDF INVERSE ALGORITHM

We now outline an inverse algorithm to quickly reconstruct image of a medium from acquired measurements using the above CFM. The model, neglecting the irrelevant parameters, can be briefly written as

$$Y(\vec{r}_d, \vec{r}_s, z_d, z_s)$$
$$= \int d\vec{r} \, dz \, W(\vec{r}_d - \vec{r}, \vec{r}_s - \vec{r}, z, z_d, z_s) X(\vec{r}, z) \quad (23)$$

where $\vec{R} = (\vec{r}, z)$ is the position of a voxel inside turbid medium; $\vec{r}$ is (x, y) coordinates; $\vec{R}_s = (\vec{r}_s, z_s)$ is the position of a source; and $\vec{R}_d = (\vec{r}_d, z_d)$ is the position of a detector. In (23), $Y(\vec{r}_d, \vec{r}_s, z_d, z_s)$ is the measured change in light intensity received by a detector at $\vec{R}_d$ from a point source at $\vec{R}_s$. $X(\vec{r}, z)$ is the change of the optical parameters inside turbid medium. The weight function $W(\vec{r}_d - \vec{r}, \vec{r}_s - \vec{r}, z, z_d, z_s)$ is a function of $\vec{r}_d - \vec{r}$ and $\vec{r}_s - \vec{r}$ on (x, y) plane, because of parallel geometry, assuming an infinite sized area, and the 2-D translation invariance of the Green's function in a background homogeneous slab. Here, the special form of the weight function is not relevant; the weight function can be calculated by the CFM or the DA models, using with CW, frequency, or time-resolved data. This approach is general and can also be used for inverse problems of nonoptical measurements in parallel geometries.

A light source scans through a 2-D array. Transmitted or backscattered light signals emerging from the medium are detected using a 2-D array of detectors, such as a charge-coupled device (CCD) camera (or time-gated CCD camera in the time resolved case). Each illumination of the light source provides a set of 2-D data on the 2-D detector array. For CW or frequency-modulated light source, this arrangement can produce a set of 2-D × 2-D = 4-D data in a relatively short acquisition time, because a CCD camera produces 2-D data of the detectors at different positions simultaneously. When time-resolved or modulation at multiple frequencies are applied, a set of five-dimensional (5-D) data can be acquired. The inverse problems of 3-D imaging, hence, are over-determined, which is necessary for obtaining an accurate 3-D image.

When the translation invariance is satisfied, the Fourier transform approach is a powerful technique to achieve a fast inversion. In the Fourier space, the convolution of W and X becomes a product of W and X, and the weight matrix W becomes diagonal. Hence, inversion can be performed much faster. Using this concept in the case of multiple sources and

multiple detectors in parallel geometries a dual 2-D Fourier transform $\int d\vec{r}_s \, d\vec{r}_d e^{i\vec{q}_s \vec{r}_s} e^{i\vec{q}_d \vec{r}_d}$ is performed on (23), to obtain

$$\int d\vec{r}_s \, d\vec{r}_d e^{i\vec{q}_s \vec{r}_s} e^{i\vec{q}_d \vec{r}_d} Y(\vec{r}_s, \vec{r}_d, z_s, z_d)$$
$$= \int dz \int d\vec{r} \int d(\vec{r}_s - \vec{r}) \, d(\vec{r}_d - \vec{r}) e^{i\vec{q}_s \cdot (\vec{r}_s - \vec{r})} e^{i\vec{q}_d (\vec{r}_d - \vec{r})}$$
$$\cdot W(\vec{r}_s - \vec{r}, \vec{r}_d - \vec{r}, z_s, z_d, z) e^{i(\vec{q}_s + \vec{q}_d)\vec{r}} X(\vec{r}, z)$$

which leads to

$$\hat{Y}(\vec{q}_d, \vec{q}_s, z_d, z_s) = \int dz \hat{W}(\vec{q}_d, \vec{q}_s, z, z_d, z_s) \hat{X}(\vec{q}_d + \vec{q}_s, z) \quad (24)$$

where $\hat{Y}$, $\hat{X}$, and $\hat{W}$ are change in light intensity, change in optical parameters, and the weight function in the Fourier space, respectively.

A similar form of this dual Fourier transform has been derived by Markel and Schotland [13], [14] in a frequency-domain diffusion model.

Equation (24) seems difficult to be used for performing the inverse reconstruction because of the argument mismatch ($\vec{q}_d + \vec{q}_s$) in $\hat{X}$ and ($\vec{q}_s, \vec{q}_d$) in $\hat{Y}$ and $\hat{W}$. This difficulty occurs because the weight function in (23) is related to three positions: $\vec{r}_d$, $\vec{r}_s$, and $\vec{r}$. To remove this complexity, the following linear hybrid transform is introduced:

$$\vec{u} = \vec{q}_d + \vec{q}_s$$
$$\vec{v} = \vec{q}_d - \vec{q}_s. \quad (25)$$

This results in the HDF formula

$$\tilde{Y}(\vec{u}, \vec{v}, z_d, z_s) = \int dz \tilde{W}(\vec{u}, \vec{v}, z, z_d, z_s) \tilde{X}(\vec{u}, z) \quad (26)$$

where $\tilde{Y}$, $\tilde{X}$, and $\tilde{W}$ are, respectively, $\hat{Y}$, $\hat{X}$, and $\hat{W}$ as functions of $\vec{u}$ and $\vec{v}$.

While (25) is a relatively simple expression, it is essential to properly realize this hybrid transform in discrete lattices of the Fourier space. A procedure to quickly perform this transform from (q_d, q_s) coordinates to new (u, v) coordinates, separately, for x and y components, is explained in Fig. 5 using an example of a 6 × 6 lattice. The maximum value of u is taken as the maximum value of q_d or q_s, not the maximum value of $q_d + q_s$. The periodic property of lattice in the Fourier space is used, for example, $\tilde{Y}(u = 2, v = 4) = \hat{Y}(q_s = 3, q_d = 5)$. This procedure builds a one-to-one correspondence between lattices in the two coordinate systems. Fig. 5 shows that $\tilde{Y}$ and $\tilde{W}$ at each node [circle in Fig. 5] in (u, v) coordinates are directly mapped from $\hat{Y}$ and $\hat{W}$, respectively, at the corresponding node in (q_d, q_s) coordinates without any algebraic manipulation.

In (26), a common 2-D Fourier argument $\vec{u}$ appears in $\tilde{Y}$, $\tilde{X}$, and $\tilde{W}$. For each value of $\vec{u}$, (26) leads to an over-determined 1-D problem for inverse reconstruction: $\tilde{Y}(\vec{v}) = \int dz \tilde{W}(\vec{v}, z) \tilde{X}(z)$. In order to perform fast inversion, we invert the normal form of the forward model: $\tilde{Y}\tilde{W}^T = [\tilde{W}^T \tilde{W}]\tilde{X}$ for each $\vec{u}$, where $[\tilde{W}^T \tilde{W}]$ is a $M \times M$ matrix, with M the number of layers in z direction. The original W in (23) is a matrix with a large dimension. The inverse
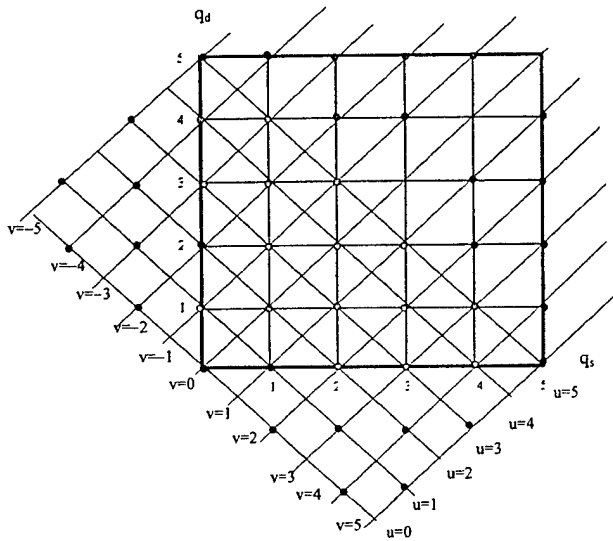
Fig. 5. Example of a 6 × 6 lattice for explaining the linear hybrid transform from (q_d, q_s) coordinates to (u, v) coordinates.

Fig. 6. 3-D image reconstructed using hybrid dual Fourier tomography. Two absorbing objects, each with the volume 3 × 3 × 2 mm³, are located inside a turbid medium with volume 96 × 96 × 40 mm³ divided into 32 × 32 × 20 voxels. The first one is located at position labeled (10, 10, 10) with absorption difference $\Delta\mu_a = 0.01$ mm⁻¹. The second one is located at position labeled (20, 20, 15) with absorption difference $\Delta\mu_a = 0.007$ mm⁻¹. A CW light source incident perpendicular to the $z_s = 0$ plane is scanned through a 2D 32 × 32 array at the plane, with each pixel 3 mm × 3 mm. A same sized 2D array of detectors is located at z_d plane (transmission geometry). The simulated data are produced with noise 5%. A linear scale of color bar from the maximum value to minimum value of $\Delta\mu_a$ is used. The numbers labels the z layers counting form source to the detector, layers are separated by 2 mm.

problem now is simplified to invert many (number of discrete value of $\vec{u}$) matrices, each with a small dimension M. The latter problem is much more computationally efficient compared to the original problem of (23). Once $\tilde{X}(\vec{u}, z)$ are obtained for all $\vec{u}$, a 2-D inverse Fourier transform produces $X(\vec{r}, z)$, which is the 3-D image of optical parameters of the medium. Markel and Schotland use different procedures for inversion. In [13], a Fourier–Laplace inversion is applied, hence, an analytic continuation of measured data to the complex plane is required for the inverse Laplace transform. In [14], an inverse procedure is performed in an argument space, similar to variables $\vec{v}$ here. Since $\vec{v}$ include 2-D variables, inversion in $\vec{v}$ space could take longer time than that of inversion in z space.

As discussed previously, matrices $\tilde{W}$ and $[\tilde{W}^T\tilde{W}]$ for each $\vec{u}$ can be calculated in advance for a uniform background slab medium. Assuming that a group of experimental data has been acquired, the following steps are taken to produce a 3-D image of the medium:

1) obtain "change" of intensities, $Y(\vec{r}_d, \vec{r}_s, z_d, z_s)$, by subtracting the intensity for a uniform background medium from the measured intensity;

2) extend the (x, y) area and padding zeros, to overcome the wraparound problem in discrete convolutions [19];

3) perform a dual 2-D fast Fourier transform (FFT) of $Y(\vec{r}_d, \vec{r}_s, z_d, z_s)$ in the extended area to produce $\hat{Y}(\vec{q}_d, \vec{q}_s, z_d, z_s)$;

4) determine $\tilde{Y}(\vec{u}, \vec{v}, z_d, z_s)$ for each $\vec{u}$, using a mapping procedure explained in Fig. 5;

5) invert $\tilde{Y}\tilde{W}^T = [\tilde{W}^T\tilde{W}]\tilde{X}$ for each $\vec{u}$, which is an inverse problem involving a $M \times M$ matrix, with M the number of layers along z direction. Proper regularization according to noise level needs to be taken into account. Regularization will be discussed later in the paper;

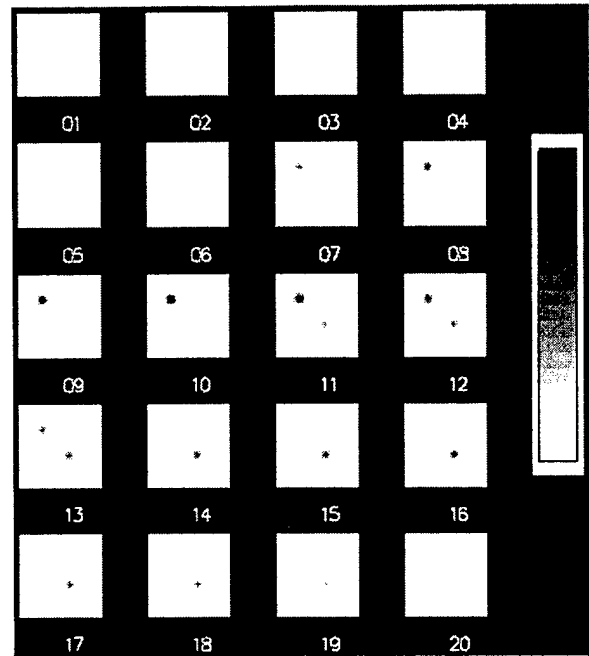6) perform an inverse 2-D FFT on $\tilde{X}(\vec{u}, z)$ to produce $X(\vec{r}, z)$.

Our computational experiments show it takes only 1–2 min on a personal computer to perform an inverse reconstruction of a 3-D image of a medium with a large number of voxels (for example, 32 × 32 × 20 voxels) using this HDF algorithm.

To demonstrate our concept of HDF tomography in 3-D image reconstruction, an example using simulated CW data is presented. A slab turbid medium, with a transport mean-free path $l_{tr} = 1$ mm, absorption length $l_a = 300$ mm, and thickness $z_d = 40$ mm, is divided into 20 layers. A CW light source, injected perpendicular to the $z_s = 0$ plane, scans by a 2-D 32 × 32 array on the plane, with each pixel 3 × 3 mm. A 2-D array of detectors with the same spacing is located at z_d plane (transmission geometry). The medium, is divided into 32 × 32 × 20 voxels, each of dimension 3 × 3 × 2 mm³. Two absorbing objects are located in the medium, each with a volume 3 × 3 × 2 mm³. The first one located at (10, 10, 10) has an absorption difference of $\Delta\mu_a = 0.01$ mm⁻¹ with the background. The second one is located at (20, 20, 15) with an absorption difference of 0.007 mm⁻¹. The simulated data with noise level of 5% are obtained using the CFM. The tomographic images are shown in Fig. 6. As shown, the central positions of 3-D image of the objects are correct, located at a voxel (10, 10, 10) with dark color, and a voxel (20, 20, 15) with gray level. The resolution of image is about ~6 mm in the transverse

(x, y) plane and ~10 mm along z direction. In general, the axial resolution (along z direction) is poorer than the lateral resolution [on the (x, y) plane]. In transmission geometry, two Green's functions in the weight function compensate each other when the z position of the object changes, that leads to a poor sensitivity of the measured photon intensity to the z position of the object. The shapes of 3-D image of two objects are ellipsoids with longer axis along the z direction. The absorption difference has the maximum value at the center of ellipsoid, and decays gradually with increase distance from the center.

A cutoff in discrete lattices of $\vec{q}_s$ and $\vec{q}_d$ naturally introduces a kind of regularization. This regularization is very effective. Initial tests show that even adding 30% of fluctuations on simulated data of $Y(\vec{r}_d, \vec{r}_s, z_d, z_s)$, an image similar to that shown in Fig. 6 is still reconstructed. The reason for this is that noises come from fluctuations at different source and detector positions, which are mainly the high-frequency components of $\vec{q}_s$ and $\vec{q}_d$. A cutoff in $\vec{q}_s$ and $\vec{q}_d$ naturally eliminates these high frequency noises, such that a stable image, especially in (x, y) plane, can be reconstructed in a strong noise level.

However, the inverse problem is still ill-posed, because contribution to the change of intensity from a small voxel deeply inside medium is weak, and is not sensitive to its z position in transmission case. A regularization procedure on inversion of $\tilde{Y}\tilde{W}^T = [\tilde{W}^T\tilde{W}]\tilde{X}$ is still needed. The standard Tikhonov regularization approach [20] is applied and L-curve [21], [22] method is used for determining the best regularization parameters.

This fast inverse algorithm produces a 3-D image in a linear image regime. For nonlinear image reconstruction procedure, the reconstructed 3-D image provides a good initial profile for further refining the 3-D image taking the nonlinear effects into consideration.

The HDF inversion method can be extended to a cylindrical geometry, with an arbitrary shape of the (x, y) cross section, for 3-D image reconstruction. In this geometry, an algorithm using a single Fourier inversion has been developed [23]. This algorithm is limited to the case that the sources and the detectors are located on a plane with same z coordinates. The hybrid-dual-Fourier inverse approach in cylindrical geometry removes this restriction, so more data can be acquired for 3-D tomography. The linear forward model in cylindrical geometry is given by

$$Y(\vec{r}_d, \vec{r}_s, z_d, z_s)$$
$$= \int d\vec{r} dz W(\vec{r}_d, \vec{r}_s, \vec{r}; z_d - z, z_s - z) X(\vec{r}, z) \quad (27)$$

where $W(\vec{r}_d, \vec{r}_s, \vec{r}; z_d - z, z_s - z)$ is the weight function, a function of $z_d - z$ and $z_s - z$ due to the 1-D translation invariance of the Green's function in a homogeneous background medium in cylindrical geometry (assuming infinite z length). We make a dual 1-D (along z direction) Fourier transform $\int dz_d dz_s e^{iq_d z_d} e^{iq_s z_s}$ on (27) to obtain

$$\hat{Y}(q_d, q_s, \vec{r}_d, \vec{r}_s) = \int dz \hat{W}(q_d, q_s, \vec{r}, \vec{r}_d, \vec{r}_s) \hat{X}(q_d + q_s, \vec{r})$$
$$(28)$$

where $\hat{Y}$, $\hat{X}$, and $\hat{W}$ are the Fourier space quantities corresponding that in (27).

The (1-D) linear hybrid coordinate transforms, $u = q_d + q_s$, and $v = q_d - q_s$, for (28) leads to

$$\tilde{Y}(u, v, \vec{r}_d, \vec{r}_s) = \int d\vec{r} \tilde{W}(u, v, \vec{r}_d, \vec{r}_s; \vec{r}) \tilde{X}(u, \vec{r}) \quad (29)$$

where $\tilde{Y}$, $\tilde{X}$, and $\tilde{W}$ are, respectively, $\hat{Y}$, $\hat{X}$, and $\hat{W}$ as functions of u and v. For each value of u, (29) is an over determined 2-D problem for inverse reconstruction, namely, to determine a 2-D unknown value of $\tilde{X}(u, \vec{r})$ from known 3-D data of $\tilde{Y}(u, v, \vec{r}_d, \vec{r}_s)$ for each u. This 3-D–2-D determination enhances the accuracy of 3-D image compared to 2-D–2-D determination in the single-Fourier transform inversion. After $\tilde{X}(u, \vec{r})$ are obtained for all u, a 1-D inverse Fourier transform produces the image $X(\vec{r}, z)$.

V. DISCUSSION

As shown in (19) and (21), there is no contribution from s wave to the weight function for a scattering object. This result reflects a fact that no scattering effect exists for an isotropic angular distribution. In the regions far from sources, the weight function contributed from scattering objects is small because there is no contribution from the dominant s wave, as shown in many results based on the diffusion models [1]–[5]. This non-sensitivity of signals to the scattering objects deep inside the medium should be considered in optical tomography. A pure isotropic distribution is never achieved, otherwise, there will be no flux in any directions. In the diffusive model, a small p wave, $-(3/4\pi)D\mathbf{s} \cdot \nabla N$, exists which maintains the photons diffusing to the regions with fewer photons. The factor $-\nabla N$ represents this effect. However, this expression is valid only in the regions where the p wave is much smaller than s wave, $(1/4\pi)N$, and does not correctly describe the early photon propagation near sources. Since only the weight function for scattering objects close to sources plays an important role, but it was estimated using the formula valid in regions far from sources, substantial error introduced in the diffusion forward model for scattering objects is crucial, considering $\mu_s' \gg \mu_a$ in tissue.

For the weight function of absorbing objects, contributions from all spherical components, including s wave, are given in (18) and (20). In commonly used diffusion formula, the contribution from p wave was neglected. The diffusion coefficient originally derived in the DA is $D = 1/(3\mu_s' + \mu_a)$, that leads to $\Delta D = -D^{(0)2}(3\Delta\mu_s' + \Delta\mu_a)$. The contribution from p wave to the weight function for absorbing objects, hence, should exist. However, in the later diffusion models, ΔD is assigned only for scattering objects and only s wave for absorbing objects is taken. Equations (18) and (20) provide a quantitative estimation of weight function for absorbing objects in regions close to the source, as well as far from the source.

The CFM and the HDF inverse algorithm need further improvements in the following aspects. Further improvement should be considered without significantly increasing complexity in computation. First, the second cumulant solution is not accurate in the detailed shape of the distribution, especially, the front edge in the Gaussian distribution violates causality. An empirical distribution, which keeps the exact value of the first and second cumulants, while satisfies the causality, can be designed to replace the Gaussian distribution.

Second, the boundary condition is approximate. When a more accurate distribution $I(\mathbf{r}, \mathbf{s}, t)$ at early time is needed, the boundary condition for a semi-infinite geometry should be

$$I(x, y, z = 0; \theta, \phi, t) = 0, \qquad \text{if } \cos\theta > 0. \quad (30)$$

This type of the boundary condition was studied by Domke [24] for the steady state case. The solution is represented as a superposition of a solution describing a transport problem in an infinite medium, and a Fredholm integral term, which corrects this solution for the appropriate half-space boundary condition. This approach may be used for further development of the boundary problem.

Third, to consider the nonlinear effects, $I^{(0)}$s in (16) should be replaced by the Green's function in a real heterogeneous medium. Among the high-order perturbative corrections of the Green's function, the "self-energy" diagram, which counts photon round trips through a position up to infinite times, plays an important role. Gandjbakhche et al. [25] studied this effect using a random walk model. We find that a renormalization procedure for this nonlinear effect can be performed after image is obtained using a linear inversion process. This renormalization procedure can recover the optimal value of the optical parameters and can improve the resolution of image. The detailed results of the renormalization will be published elsewhere.

The translation invariance is valid for the parallel geometry assuming that the (x, y) area is infinite. We suppose that this assumption of the infinite area is reasonable. How much error arises due to the finite area of a sample will be studied in details.

Use of the simulated data mainly tests the validity of the inverse algorithm, does not test accuracy of the forward model. Experimental data from phantoms and in vivo measurements in human body will be performed for further testing of our approach.

ACKNOWLEDGMENT

REFERENCES

[1] A. G. Yodh, B. Tromberg, E. Sevick-Muraca, and D. Pine, Eds., "Diffusion photons in turbid media," in *Special Issue J. Opt. Soc. A.*, 1997, vol. 14, pp. 136–342.

[2] S. R. Arridge, "Optical tomography in medical imaging," *Inv. Probl.*, vol. 15, pp. 41–93, 1999.

[3] N. Iftimia and H. Jiang, "Quantitative optical image reconstruction of turbid media using dc measurements," *Appl. Opt.*, vol. 39, pp. 5256–5261, 2000.

[4] B. W. Pogue, S. P. Poplack, T. O. McBride, W. A. Wells, U. L. Osterberg, and K. D. Paulsen, "Quantitative hemoglobin tomography with diffuse near infrared spectroscopy: Pilot results in the breast," *Radiology*, vol. 218, pp. 261–266, 2001.

[5] J. C. Hebden, H. Veenstra, H. Dehghani, E. M. C. Hillman, M. Schweiger, S. R. Arridge, and D. T. Delpy, "Three dimensional time-resolved optical tomography of a conical breast phantom," *Appl. Opt.*, vol. 40, pp. 3278–3287, 2001.

[6] H. Hielscher, R. E. Alcouffe, and B. L. Barbour, "Comparison of finite-difference transport and diffusion calculation for photon migration in homogeneous and heterogeneous tissues," *Phys. Med. Biol.*, vol. 43, pp. 1285–1302, 1998.

[7] T. Vilhunen, M. Vanhkonen, V. Kolchmainen, and J. P. Kaipio, "Linking the radiative transfer equation and the diffusion approximation," in *Proc. Dig. OSA Biomedical Topical Meeting*, 2002, pp. 12–14.

[8] W. Cai, M. Lax, and R. R. Alfano, "Cumulant solution of the elastic Boltzmann transport equation in an infinite uniform medium," *Phys. Rev. E, Stat. Phys. Plasmas Fluids Relat. Interdiscip. Top.*, vol. 61, pp. 3871–3876, 2000.

[9] ——, "Analytical solution of the elastic Boltzmann transport equation in an infinite uniform medium using cumulant expansion," *J. Phys. Chem.*, vol. B104, pp. 3996–4000, 2000.

[10] C. L. Matson, N. Clark, L. McMackin, and J. S. Fender, "Three-dimensional tumor localization in thick tissue with the use of diffuse photon-density waves," *Appl. Opt.*, vol. 36, pp. 214–220, 1997.

[11] X. D. Li, T. Durduran, A. G. Yodh, B. Chance, and D. N. Pattanayak, "Diffraction tomography for biochemical imaging with diffuse-photon density waves," *Opt. Lett.*, vol. 22, pp. 573–575, 1997.

[12] J. C. Schotland and V. A. Markel, "Inverse scattering with diffusing wave," *J. Opt. Soc. Amer. A*, vol. 18, pp. 2767–2777, 2001.

[13] V. A. Markel and J. C. Schotland, "Inverse problem in optical diffusion tomography. I Fourier–Laplace inversion formulas," *J. Opt. Soc. Amer. A*, vol. 18, pp. 1336–1347, 2001.

[14] ——, "Inverse scattering for the diffusion equation with general boundary conditions," *Phys. Rev. E, Stat. Phys. Plasmas Fluids Relat. Interdiscip. Top.*, vol. 64 035601, pp. 1–4, 2001.

[15] M. E. Zevallos, A. Ya Polischuck, B. B. Das, F. Liu, and R. R. Alfano, "Time-resolved photon-scattering measurements from scattering media fitted to noneuclidean and conventional diffusion models," *Phys. Rev. E, Stat. Phys. Plasmas Fluids Relat. Interdiscip. Top.*, vol. 57, pp. 7244–7253, 1998.

[16] M. S. Patterson, B. Chance, and B. C. Wilson, "Time-resolved reflectance and transmittance for the noninvasive measurement of tissue optical properties," *Appl. Opt.*, vol. 28, pp. 2331–2336, 1989.

[17] M. Xu, W. Cai, M. Lax, and R. R. Alfano, "Photon migration in turbid media using a cumulant approximation to radiative transfer," *Phys. Rev. E, Stat. Phys. Plasmas Fluids Relat. Interdiscip. Top.*, vol. 65 066609, pp. 1–10, 2002.

[18] L. G. Henyey and J. L. Greenstein, "Diffuse radiation in the galaxy," *Astrophys. J.*, vol. 93, pp. 70–83, 1941.

[19] W. H. Press, B. P. Flannery, S. A. Teukolsky, and W. T. Vetterling, *Numerical Recipes*. Cambridge, U.K.: Cambridge Univ. Press, 1986, pp. 407–412.

[20] A. N. Tikhonov and A. V. Groncharsky, Eds., *Ill-Posed Problems in the Natural Sciences*. Moscow, USSR.: MIR, 1987.

[21] P. Hansen and D. O'Leavy, "The use of the L-curve in the regularization of discrete ill-posed problems," *SIAM J. Sci. Comput.*, vol. 14, pp. 1487–1503, 1993.

[22] W. Cai, S. K. Gayen, M. Xu, M. Zevallos, M. Alrubaiee, M. Lax, and R. R. Alfano, "Optical tomographic image reconstruction from ultrafast time-sliced transmission measurements," *Appl. Opt.*, vol. 38, pp. 4237–4246, 1999.

[23] W. Cai, B. B. Das, F. Liu, F. A. Zeng, M. Lax, and R. R. Alfano, "Three dimensional image reconstruction in highly scattering turbid media," in *Proc. SPIE*, 1997, paper 2979, pp. 241–248.

[24] H. Domke, "Reduction of radiative transfer problems in semi-infinite media to linear Fredholm integral equations," *J. Quant. Spectrosc. Radiat. Trans.*, vol. 16, pp. 973–981, 1976.

[25] A. H. Gandjbakhche, R. F. Bonner, R. Nossal, and G. H. Weiss, "Absorptivity contrast in transillumination imaging of tissue abnormalities," *Appl. Opt.*, vol. 35, pp. 1767–1774, 1996.

ELSEVIER

More on patterns in Mie scattering

M. Xu *, R.R. Alfano

Institute for Ultrafast Spectroscopy and Lasers, New York State Center of Advanced Technology for Ultrafast Photonic Materials and Applications, and Department of Physics, The City College and Graduate Center of City University of New York, New York, NY 10031, USA

Abstract

The powerlaw patterns in Mie scattering (the normalized light intensity $I(\theta)/I(0)$ vs. the dimensionless qR where $q = 4\pi\lambda^{-1}\sin\frac{\theta}{2}$ is the magnitude of the wave vector transfer at the scattering angle θ for wavelength λ, and R is the radius of the nonabsorbing sphere with a relative refractive index $m > 1$) are analyzed using the geometrical optics approximation for particles of a large size parameter. The $(qR)^{-4}$ powerlaw regime is shown to be present only in Mie scattering of soft particles. The $(qR)^{-2}$ powerlaw regime occurs at the scattering angles of the $p = 1$ geometrical ray (refracted without internal reflections) from the portion of the incident beam with an incidence angle around $\pi/4$ upon the particle. The $(qR)^{-2}$ powerlaw regimes from particles sharing one common relative refractive index but differing in size parameters are collinear. Simple analytical expressions are derived to describe these powerlaw regimes of Mie scattering.
© 2003 Elsevier B.V. All rights reserved.

The study of light scattering by small particles is important in noninvasive characterization of small particles and radiative transfer in turbid media including atmosphere, marine environment and tissues (see, for example, van de Hulst's classic work[1] and the recent review volume edited by Mishchenko, Hovenier and Travis [2]). Light scattering from a sphere of arbitrary size and refractive index (Mie scattering), one of a few exactly solvable cases, was derived in 1908 [3]. This exact solution was given in the form of a slow converging partial-wave series involving complex functions. The physical meaning and interpretation of the Mie scattering was itself of lasting interests [4–7].

Recently, work on powerlaw regimes in Mie scattering was obtained by Sorensen and Fischbach [8] when plotting the normalized light intensity $I(\theta)/I(0)$ versus the dimensionless

* Corresponding author. Tel.: +1-212-650-6865; fax: +1-212-650-5530.

E-mail address: minxu@sci.ccny.cuny.edu (M. Xu).

parameter qR, where $q = 4\pi\lambda^{-1}\sin\frac{\theta}{2}$ is the magnitude of the wave vector transfer at the scattering angle θ for wavelength λ after ignoring the interference ripple structure. These patterns were attributed to the structure factor of the illuminated portion of the scattering object. The Fourier transform of the illuminated annular shell for a sphere of radius R was used to explain the emerging $(qR)^0$, $(qR)^{-2}$ and $(qR)^{-4}$ powerlaw regimes. This approach ignores the extra phase shift incurred to the light when it passes through the particle. The implicit assumption made there [8] that the phase shift due to the nonunity refractive index of the particle is negligible is valid for scattering of X-rays [9], but it is inappropriate for optical light scattering from particles with a large phase shift.

In this paper, we analyze patterns in Mie scattering using the geometrical optics approximation (GOA) for particles of a large size parameter and derive simple analytical expressions to describe these powerlaw regimes of Mie scattering.

The increase of the phase shift accompanies with the increase of the size parameter. The GOA becomes a viable one when the size parameter $x = kR \gg 1$ where $k = 2\pi\lambda^{-1}$ is the wave number. The scattering amplitude of light is composed of a diffraction light component and reflected and refracted rays when the contribution from surface waves can be neglected [10,1]. The diffraction peak is highly concentrated around the exact forward direction within angle $\Delta\theta \sim 1/x$. By ignoring the interference ripple structure, the Mie scattering in near forward scattering directions and outside the diffraction peak for soft particles whose refractive index m is close to unity ($|m - 1| \ll 1$) and for dense particles ($m \sim 1.5$) in GOA is dominated by the $p = 1$ geometrical ray (refracted without internal reflections) [10–12]. The $(qR)^{-2}$ and $(qR)^{-4}$ powerlaw regimes can be recovered from the asymptotic behavior of the contribution from this $p = 1$ geometrical ray [see Fig. 1].

The magnitude of the scattering amplitude of perpendicular polarization with respect to the scattering plane which was examined in [8] (the parallel polarization case can be analyzed in a
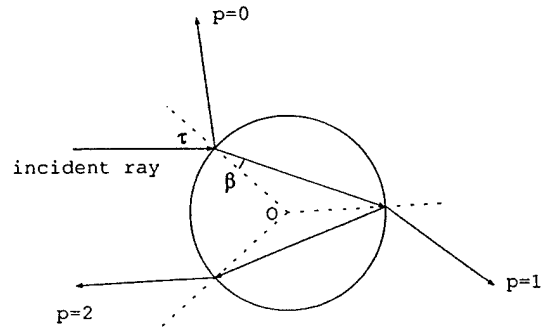

Fig. 1. Geometrical rays scattered by a sphere.

similar fashion) is dominated by the contribution A_{R_1} from the $p = 1$ geometrical ray [10]

$$|S_1(\theta)| \simeq A_{R_1}$$
$$= \frac{2mx\left(\sqrt{m^2 + (m^2 - 1)t^2}\right)^{3/2}\left(\sqrt{m^2 + (m^2 - 1)t^2} - 1\right)}{(m^2 - 1)^2(1 + t^2)^{3/2}\left(\sqrt{m^2 + (m^2 - 1)t^2} + t^2\right)^{1/2}} \tag{1}$$

and the scattering angle θ is expressed as

$$\sin\frac{\theta}{2} = \frac{t\left(\sqrt{m^2 + (m^2 - 1)t^2} - 1\right)}{m(1 + t^2)} \tag{2}$$

in terms of the incidence angle τ where $t = \tan\tau$.

For soft particles, Eqs. (1) and (2) can be expanded in powers of $\mu \equiv m - 1$

$$A_{R_1} = \frac{x}{2}\left[\frac{1}{1 + t^2}\mu^{-1} + 1 + \mathcal{O}(\mu)\right], \tag{3}$$

$$\sin\frac{\theta}{2} = \mu t + \mathcal{O}(\mu^2), \tag{4}$$

yielding

$$A_{R_1} \simeq \frac{x}{2}\frac{\mu}{\mu^2 + \sin^2\frac{\theta}{2}} \simeq \frac{x}{2}\frac{\mu}{\sin^2\frac{\theta}{2}} \tag{5}$$

under the condition $\mu \ll \sin\frac{\theta}{2} \ll \sqrt{\mu}$. The first approximate form in (5) appeared in the classic book of van de Hulst [1, p. 222].

When $\sin\frac{\theta}{2} \sim \mu$, the incidence angle τ is around $t = \tan\tau = 1$, Eqs. (1) and (2) can also be expanded about this point $t = 1$

$$A_{R_1} = \frac{\sqrt{2}mx}{m^2-1}\left(\frac{\sqrt{2m^2-1}}{\sqrt{2m^2-1}+1}\right)^{3/2}$$

$$\times\left\{1 - \frac{1}{2}\left[1 + \frac{m^2+1}{\sqrt{2m^2-1}(\sqrt{2m^2-1}+1)}\right.\right.$$

$$\left.\left.\times\frac{1}{\sqrt{2m^2-1}}\right](t-1)\right\}, \tag{6}$$

$$\sin\frac{\theta}{2} = \frac{\sqrt{2m^2-1}-1}{2m}$$

$$\times\left\{1 + \frac{1}{2}\left[1 + \frac{1}{\sqrt{2m^2-1}}\right](t-1)\right\}. \tag{7}$$

Since the refractive index $m \sim 1$,

$$\frac{m^2+1}{\sqrt{2m^2-1}(\sqrt{2m^2-1}+1)} \sim 1$$

for soft particles, and the two values inside the brackets of (6) and (7) are close even for dense particles, we find

$$A_{R_1} \simeq \frac{\sqrt{2}x}{\sin\frac{\theta}{2}}\frac{(\sqrt{2m^2-1})^{3/2}}{(\sqrt{2m^2-1}+1)^{5/2}}. \tag{8}$$
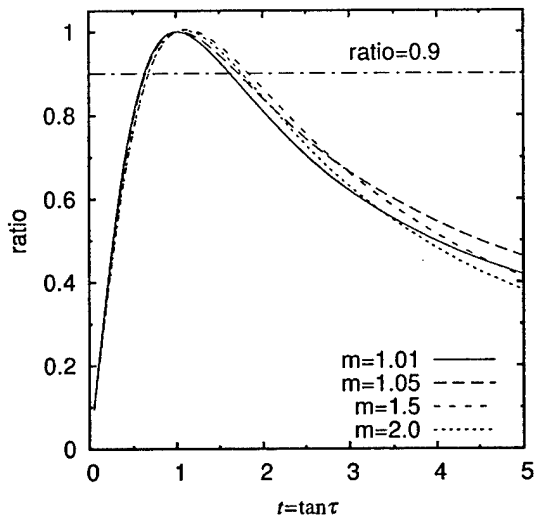
Fig. 2. The ratio $(A_{R_1}\sin\frac{\theta}{2})/(A_{R_1}\sin\frac{\theta}{2})_{t=1}$ versus $t = \tan\tau$. The curves obtained for particles of different refractive indices intersect with the 90% line at $t \simeq 0.7$ and $t \simeq 1.6$ where the value of the incidence angle is $\tau = 0.2\pi$ and $\tau = 0.3\pi$, respectively.

The range of the incidence angle τ over which the above expression (8) is valid can be examined by plotting $(A_{R_1}\sin\frac{\theta}{2})/(A_{R_1}\sin\frac{\theta}{2})_{t=1}$ versus $t = \tan\tau$ [see Fig. 2]. The range of the incidence angle is approximately $0.2\pi < \tau < 0.3\pi$ for soft and dense particles $(1 < m < 2)$ when a 10% relative error is allowed. The corresponding scattering angle range is given by

$$\frac{\sqrt{3m^2-1}-\sqrt{2}}{3m} < \sin\frac{\theta}{2} < \frac{\sqrt{35m^2-25}-\sqrt{10}}{7m}. \tag{9}$$

Thus, we can write the normalized scattered light intensity as
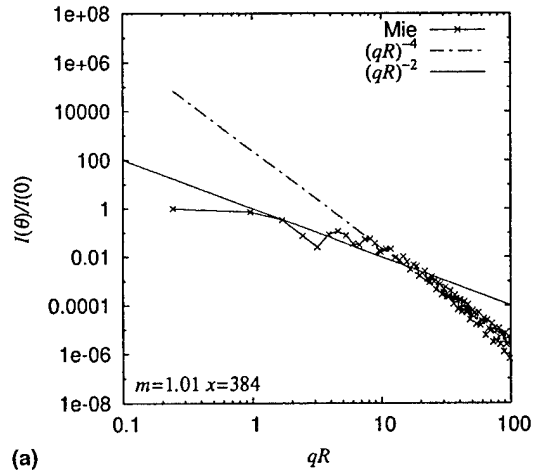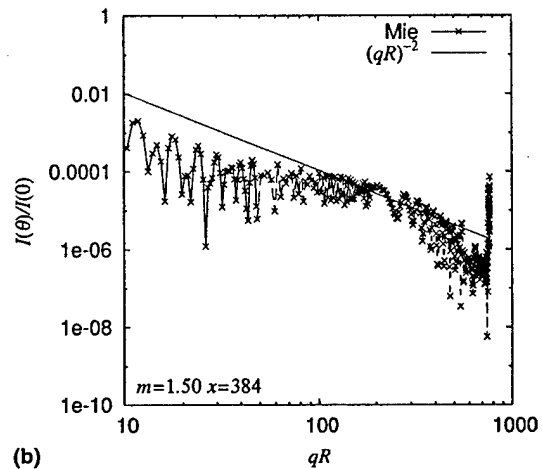
Fig. 3. The powerlaw regimes of a sphere of refractive index: (a) $m = 1.01$; (b) $m = 1.50$. The size parameter is $x = 384$.

$$\frac{I(\theta)}{I(0)} = \frac{|S_1(\theta)|^2}{|S_1(0)|^2}$$

$$\simeq \begin{cases} \frac{32(\sqrt{2m^2-1})^3}{(\sqrt{2m^2-1}+1)^5}(qR)^{-2} \\ 2k\frac{\sqrt{3m^2-1}-\sqrt{2}}{3m} < q < 2k\frac{\sqrt{35m^2-25}-\sqrt{10}}{7m} \\ 16\mu^2 x^2(qR)^{-4} \\ 2k\mu \ll q \ll 2k\sqrt{\mu}, \quad |\mu| \ll 1 \end{cases}$$

(10)

from Eqs. (5) and (8) in GOA where we have used the fact $S_1(0) = x^2/2$ and $qR = 2x\sin\frac{\theta}{2}$. This shows that the $(qR)^{-2}$ powerlaw regime exists in Mie scattering of both soft and dense particles while the $(qR)^{-4}$ powerlaw regime only appears in soft

particles. The $(qR)^{-2}$ powerlaw regimes are col-linear while the $(qR)^{-4}$ powerlaw regime are not for particles sharing one common relative refractive index but differing in size parameters. For example, the $(qR)^{-2}$ powerlaw regime is found within $5 < qR < 12$, followed by the $(qR)^{-4}$ powerlaw regime within $8 \ll qR \ll 80$, for a soft sphere of a refractive index $m = 1.01$; only the $(qR)^{-2}$ powerlaw regime is observed within $165 < qR < 300$ for the dense sphere of a refractive index $m = 1.50$ (see Fig. 3). The size parameter of the sphere in both cases is $x = 384$.

Fig. 4 demonstrated the powerlaw regimes for a nonabsorbing sphere with refractive indices
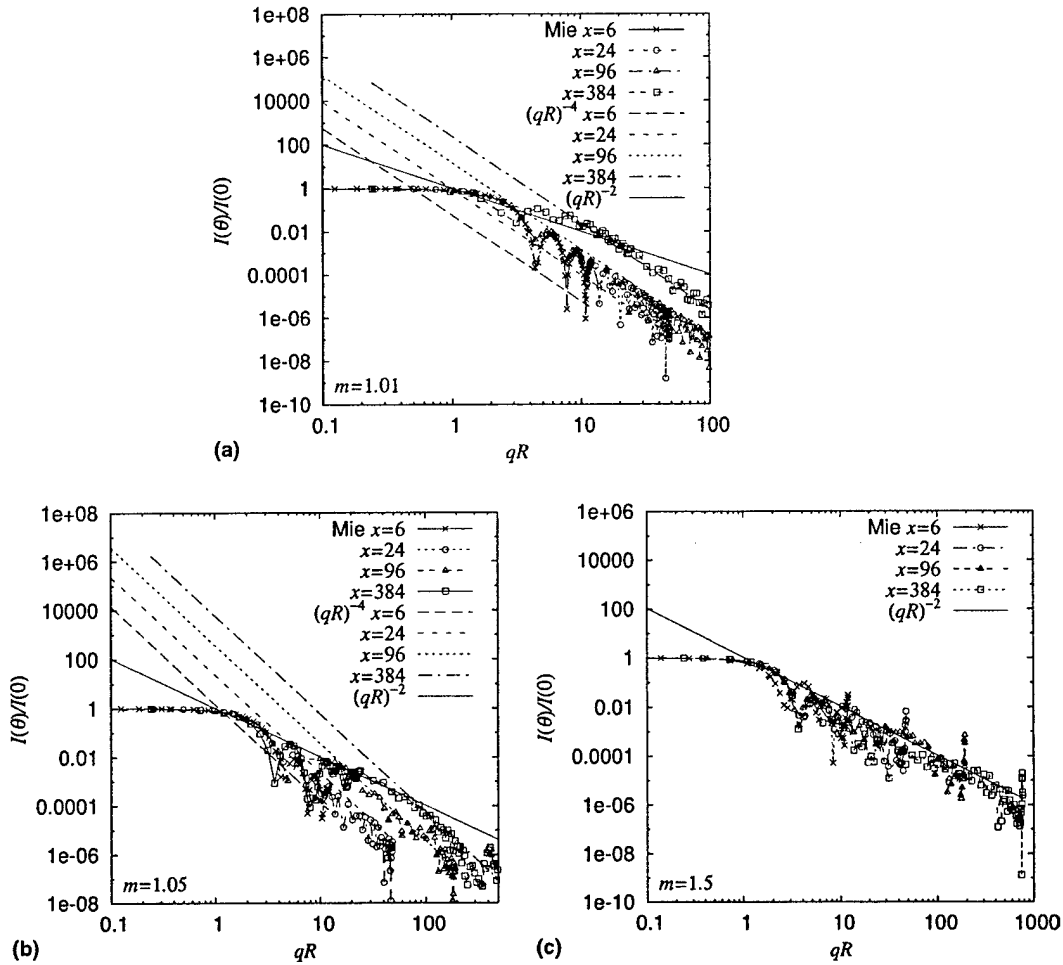

Fig. 4. The normalized Mie scattering curves plotted versus qR for spheres of refractive index: (a) $m = 1.01$; (b) $m = 1.05$; (c) $m = 1.5$. The $(qR)^{-2}$ and $(qR)^{-4}$ powerlaw regimes of Mie scattering given by Eq. (10) are also plotted.

$m = 1.01$, $m = 1.05$ and $m = 1.5$, respectively. The $(qR)^{-4}$ powerlaw regime exists only in soft particles and disappears in dense particles. Its trend agrees well with our simple expression (10) [see the long-dash, dash, dot and dash-dot lines for particles of increasing size parameters in Fig. 4(a) and (b)]. This agreement is better for larger and softer particles. On the other hand, the $(qR)^{-2}$ powerlaw regime exists in both soft and dense particles. This regime occurs at a larger value of qR for particles of a larger size parameter and is broader for denser particles. The $(qR)^{-2}$ powerlaw regimes of particles of a common refractive index but of different size parameters coincide on one straight line (the solid lines in Fig. 4(a)–(c)).

In conclusion, we have analyzed the powerlaw patterns in Mie scattering using the geometrical optics approximation for particles of a large size parameter. The $(qR)^{-4}$ powerlaw regime is shown to be present only in soft particles. The $(qR)^{-2}$ powerlaw regime occurs at the scattering angles of the $p = 1$ geometrical ray (refracted without internal reflections) from the portion of the incident beam with an incidence angle around $\pi/4$ (from 0.2π to 0.3π within a 10% relative error of the scattering amplitude) upon the particle. The $(qR)^{-2}$ powerlaw regimes from particles sharing one common relative refractive index but differing in size parameters are collinear. The $(qR)^{-2}$ and $(qR)^{-4}$ powerlaw regimes of Mie scattering are well captured by the simple analytical expressions given in Eq. (10).

Acknowledgements

References

[1] H.C. van de Hulst, Light Scattering by Small Particles, Dover, New York, 1981.

[2] M.I. Mishchenko, J.W. Hovenier, L.D. Travis (Eds.), Light Scattering by Nonspherical Particles: Theory, Measurements, and Applications, Academia Press, San Diego, 1999.

[3] G. Mie, Beitrage zur optik trüber medien speziell kolloidaler metallösungen, Ann. Phys. (1908) 377–445.

[4] H.M. Nussenzveig, W.J. Wiscombe, Efficiency factors in Mie scattering, Phys. Rev. Lett. 45 (1980) 1490–1494.

[5] H. Nussenzveig, Diffraction Effects in Semiclassical Scattering, Cambridge University Press, Cambridge, 1992.

[6] L. Guimaraes, H. Nussenzveig, Theory of mie resonances and ripple fluctuations, Opt. Commun. 89 (1992) 363–369.

[7] A.J. Baran, J.S. Foot, D.L. Mitchell, Ice-crystal absorption: a comparison between theory and implications for remote sensing, Appl. Opt. 37 (12) (1998) 2207–2215.

[8] C.M. Sorensen, D.J. Fischbach, Patterns in Mie scattering, Opt. Commun. 173 (2000) 145–153.

[9] A. Guinier, G. Fournet, C.B. Walker, K.L. Yudowitch, Small-angle scattering of X-rays, John Wiley & Sons, New York, 1955.

[10] A. Ungut, G. han, G. Gouesbet, Comparisons between geometrical optics and Lorenz–Mie theory, Appl. Opt. 20 (17) (1981) 2911–2918.

[11] E.A. Hovenac, Calculation of far-field scattering from nonspherical particles using a geometrical optics approach, Appl. Opt. 30 (33) (1991) 4739–4746.

[12] A. Macke, M.I. Mishchenko, K. Muinonen, B.E. Carlson, Scattering of light by large nonspherical particles: ray-tracing approximation versus *t*-matrix method, Opt. Lett. 20 (19) (1995) 19341936.

Nonlinear multiple passage effects on optical imaging of an absorption inhomogeneity in turbid media

M. Xu, W. Cai and R. R. Alfano

Institute for Ultrafast Spectroscopy and Lasers,
New York State Center of Advanced Technology for Ultrafast Photonic Materials and Applications,
and Department of Physics,
The City College and Graduate Center of City University of New York, New York, NY 10031

ABSTRACT

We report on the effect of the nonlinear multiple passage on optical imaging of an absorption inhomogeneity of finite size deep inside a turbid medium based on a cumulant solution to radiative transfer. An analytical expression for the nonlinear correction factor is derived. Comparison to Monte Carlo simulations reveals an excellent agreement. The implication on optical imaging is discussed.

Keywords: nonlinear correction, multiple passage, radiative transfer, optical imaging

1. INTRODUCTION

The principle of optical imaging of turbid media (such as tissues) is to locate and reconstruct the optical properties (absorption and scattering coefficients) of embedded inhomogeneities (such as tumor) in the hope of identification by inverting the difference in time-resolved or frequency-modulated photon transmittance due to the presence of the inhomogeneities through either iterative or noniterative methods. The key quantity involved is the weight function which quantifies the influence on the detected signal due to the change of the optical parameters of the medium. The diffusion approximation to radiative transfer provides an adequate model for the weight function (or Jacobian) for a small and weak absorption inhomogeneity far away from both the source and the detector. However, the weight function predicted by the linear perturbation approaches is no longer valid when the absorption strength is not small.[1] This can be attributed to the multiple passage of a photon through one single abnormal site.

The change of the light intensity ΔI at the detector r_d due to the presence of an absorption site at r from a modulated point source at r_s is expressed as

$$\Delta I = -\delta\mu_a V G(r_d, \omega | r) G(r, \omega | r_s) \tag{1}$$

to the first order of Born approximation where $\delta\mu_a$ is the excess absorption of the absorption site whose volume is V, ω is the modulation frequency of light, and G is the propagator of photon migration in the background medium. Here, the Green's function $G(r_2, \omega | r_1)$, in general, depends on the detail of light scattering inside the medium, and the incident and outgoing directions of light.

When the absorption strength is not small ($\delta\mu_a V \not\ll 1$), photon loss due to multiple passage of the absorption site is appreciable and can not be ignored. The expression for ΔI in Eq. (1) needs to be modified to include the contributions from multiple visits of the site by the photon. Fig. (1) illustrates the most important correction (a "self-energy" correction) which takes into account the repeated visits made by a photon to the site up to an infinite times.

Further author information: (Send correspondence to M. Xu)
M. Xu: Email: minxu@sci.ccny.cuny.edu

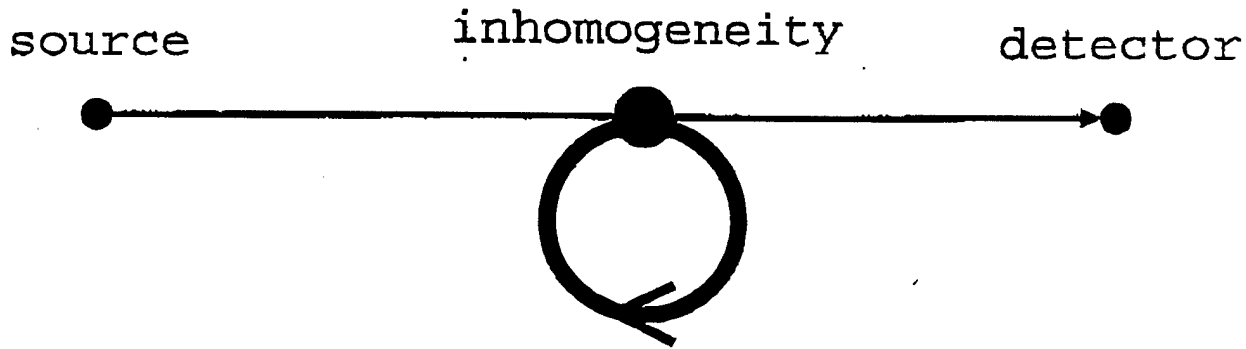**source**   **inhomogeneity**   **detector**

Figure 1. Self-energy correction to the multiple passage effect on light absorption.

Assuming that the center of the absorption site is located at $\bar{r}$ and far away from both the source and the detector, the change of the detected light, ΔI, is now given by

$$\Delta I = -G(r_d, \omega | \bar{r}) V \delta \mu_a(\bar{r}) \sum_{n=0}^{\infty} \left[-\bar{N}_{self}(\omega; R) V \delta \mu_a(\bar{r}) \right]^n G(\bar{r}, \omega | r_s) \qquad (2)$$

$$= -G(r_d, \omega | \bar{r}) \frac{V \delta \mu_a(\bar{r})}{1 + \bar{N}_{self}(\omega; R) V \delta \mu_a(\bar{r})} G(\bar{r}, \omega | r_s)$$

where

$$\bar{N}_{self}(\omega; R) = \frac{1}{V^2} \int_V \int_V G(r_2, \omega | r_1) d^3 r_2 d^3 r_1 \qquad (3)$$

is the self-propagator which describes the probability that a photon revisits the volume V of size R. Here $G(r_d, \omega | \bar{r})$ and $G(\bar{r}, \omega | r_s)$ are well modelled by the center-moved diffusion model as long as the separations $|r_d - \bar{r}|, |r_s - \bar{r}| \gg l_t$ where l_t is the transport mean free path of light in the medium.[2] However, the diffusion Green's function can not be used in Eq. (3) to evaluate $\bar{N}_{self}(\omega; R)$ where r_1 is in the proximity of r_2. By comparing Eq. (2) to Eq. (1), the nonlinear multiple passgage effect of an absorption site can be summarized by the nonlinear correction factor $[1 + \bar{N}_{self}(\omega; R) V \delta \mu_a(\bar{r})]^{-1}$. This factor serves as a universal measure of the nonlinear multiple passage effect as long as the absorption site is far away from both the source and the detector and its size is much smaller than its distance to both the source and the detector.

In this article, we will derive an analytical expression for the self-propagator to understand the nonlinear multiple passage effect on light absorption using our cumulant solution to radiative transfer. The nonlinear correction factor $[1 + \bar{N}_{self}(\omega; R) V \delta \mu_a(\bar{r})]^{-1}$ of our result is shown to be in an excellent agreement with the Monte Carlo simulations for continuous wave light.

2. THEORY

To take into account the higher order contributions from the absorption inhomogeneity, the behavior of the photon migration in a short distance must be considered. Although the photon distribution is almost isotropic at an absorption site deep inside the medium, the diffusion approximation is still not appropriate here. The separation between the two points r_1 and r_2 within the volume in Eq. (3) is small. The photon propagator $N(r_2, t | r_1, s)$, which represents the probability that a photon propagates

from position $\mathbf{r}_1$ with propagation direction $\mathbf{s}$ to position $\mathbf{r}_2$ in time t, when $\mathbf{r}_2$ is in the proximity of $\mathbf{r}_1$, is governed by the radiative transfer equation rather than the diffusion equation.

Recently we have shown that the propagation of photon inside a turbid medium (the radiative transfer equation) can be solved analytically using a cumulant expansion of the photon distribution function.[3] The propagation of photon was found to transform from an initial ballistic motion at early time and then gradually to a center-adjusted diffusion at later time. The propagator of photon density (the Green's function) in an infinite uniform medium is given by[4]

$$N(\mathbf{r}, t|\mathbf{r}_0, \mathbf{s}_0) = \frac{1}{[4\pi D(t)t]^{3/2}} \exp\left[-\frac{(\mathbf{r} - \mathbf{r}_0 - \mathbf{s}_0 \Delta(t))^2}{4D(t)t} - \mu_a t\right] \tag{4}$$

ignoring the small difference in the diffusion coefficient along different directions where the absorption coefficient is μ_a, the time-dependent diffusion coefficient is

$$D(t) = \frac{l_t^2}{3t}\left\{\frac{ct}{l_t} - [1 - \exp(-ct/l_t)] - \frac{1}{2}[1 - \exp(-ct/l_t)]^2\right\} \tag{5}$$

and

$$\Delta(t) = l_t[1 - \exp(-ct/l_t)] \tag{6}$$

is the average center of photons which moves with speed c initially and approaches the transport mean free path l_t in the long time limit. The Green's function for parallel geometries can be obtained by the method of image sources.[5]

2.1. Propagator of an isotropic point source

Let's now consider the propagator $N(\mathbf{r}, t|\mathbf{r}_0, \mathbf{s}_0)$ at the inhomogeneity site $\mathbf{r}_0 = 0$ (the origin of space) deep inside the medium. The photon distribution at $\mathbf{r}_0$ is almost isotropic but is *anisotropic* scattering. The effective propagator can then be obtained by averaging (4) over the propagation direction $\mathbf{s}_0$ of light over the 4π solid angle, and is given by [see Appendix A]

$$N_{\text{eff}}(r, t) = \frac{1}{4\pi}\int d^2\mathbf{s}_0 N(\mathbf{r}, t|\mathbf{r}_0, \mathbf{s}_0) = \frac{\exp(-\mu_a t)}{(4\pi)^{3/2}(D(t)t)^{1/2}r\Delta(t)} \tag{7}$$

$$\times\left\{\exp\left[-\frac{(r - \Delta(t))^2}{4D(t)t}\right] - \exp\left[-\frac{(r + \Delta(t))^2}{4D(t)t}\right]\right\}.$$

This reduces to

$$N_{\text{eff}}(r, t) = \frac{\exp(-\mu_a t)}{4\pi r^2}\delta(r - ct), \quad \text{for } t \to 0^+ \tag{8}$$

and

$$N_{\text{eff}}(r, t) = \frac{\exp(-\mu_a t)}{(4\pi)^{3/2}(D_\infty t)^{1/2}r l_t}\left\{\exp\left[-\frac{(r - l_t)^2}{4D_\infty t}\right] - \exp\left[-\frac{(r + l_t)^2}{4D_\infty t}\right]\right\}, \quad \text{for } t \gg 1 \tag{9}$$

in early and late time limits where $D_\infty \equiv l_t c/3$.

The temporal Fourier transforms of the asymptotic equations (8) and (9) are given by

$$N_{\text{eff}}(\mathbf{r}, \omega) = \frac{1}{4\pi r^2 c}\exp\left[(i\omega - \mu_a)\frac{r}{c}\right] \tag{10}$$

and

$$N_{\text{eff}}(\mathbf{r}, \omega) = \frac{1}{8\pi D r \kappa l_t} \left[\exp(-\kappa |r - l_t|) - \exp(-\kappa(r + l_t)) \right] \tag{11}$$

respectively, where $\kappa \equiv \sqrt{3(\mu_a - i\omega)/l_t c}$ whose sign is chosen with a nonnegative real part. In the limit of small $\kappa \ll 1$, Eq. (11) simplifies to

$$\lim_{\kappa \to 0} N_{\text{eff}}(\mathbf{r}, \omega) = \begin{cases} \frac{1}{4\pi D_\infty l_t} & r < l_t \\ \frac{1}{4\pi D_\infty r} & r \geq l_t \end{cases} . \tag{12}$$

This is the case, for example, that a continuous wave propagates in a nonabsorbing medium. The errornous divergence at the zero separation in the diffuse Green's function

$$G(r, \omega) = \frac{\exp(-\kappa r)}{4\pi D_\infty r} \tag{13}$$

is removed in our formulation of the propagation of an isotropic point source.

The asymptotic equation (11) from the late time limit provides a good approximation for $N_{\text{eff}}(r, \omega)$ when $r > l_t$ [see Fig. (2)]. The contribution to $N_{\text{eff}}(r, \omega)$ when $r < l_t$ is from either ballistic or diffusive photons, hence an improvement to Eq. (10) can be made

$$N_{\text{eff}}(r, \omega) \simeq \frac{1}{4\pi r^2 c} \exp\left[(i\omega - \mu_a)\frac{r}{c} \right] + \frac{\exp(-\kappa l_t)}{4\pi D_\infty r \kappa l_t} \sinh(\kappa r), \quad r < l_t \tag{14}$$

to include the contribution from diffusive photons. The effective propagator in temporal Fourier space $N_{\text{eff}}(r, \omega = 0)$ and its asymptotic behaviors (10), (11) and (14) are shown in Fig. (2). The diffusion Green's function has a huge error for small r.

2.2. Self propagator for a finite volume

For an absorption site of a finite volume V deep inside the medium, say a sphere of radius $R \ll L$ where L is the dimension of the medium, the self-propagator $\bar{N}_{\text{self}}(t; R)$ for this volume which denotes a photon revisits the site in time t is written as:

$$\begin{aligned} \bar{N}_{\text{self}}(t; R) &= \frac{1}{V^2} \int_V \int_V N_{\text{eff}}(|\mathbf{r}_2 - \mathbf{r}_1|, t) d^3 r_1 d^3 r_2 \\ &= \frac{1}{V} \int_0^{2R} N_{\text{eff}}(r, t) \gamma_0(r) 4\pi r^2 dr \end{aligned} \tag{15}$$

where

$$\gamma_0(r) = 1 - \frac{3r}{4R} + \frac{1}{16} \left(\frac{r}{R} \right)^3 \tag{16}$$

is the characteristic function for a uniform sphere.[6-8] This characteristic function has a form of

$$\gamma_0(r) = 1 - (S/4V)r + \dots \tag{17}$$

for an arbitrary particle where S is the surface area of the particle. This self propagator (15) for a finite volume is quite different from the self-propagator of a point, obtained by setting $r = 0$ in (4) or (7), i.e.,

$$N_{\text{eff}}(0, t) = \frac{\exp(-\mu_a t)}{(4\pi D(t)t)^{3/2}} \exp\left[-\frac{\Delta(t)^2}{4D(t)t} \right], \quad (t > 0). \tag{18}$$
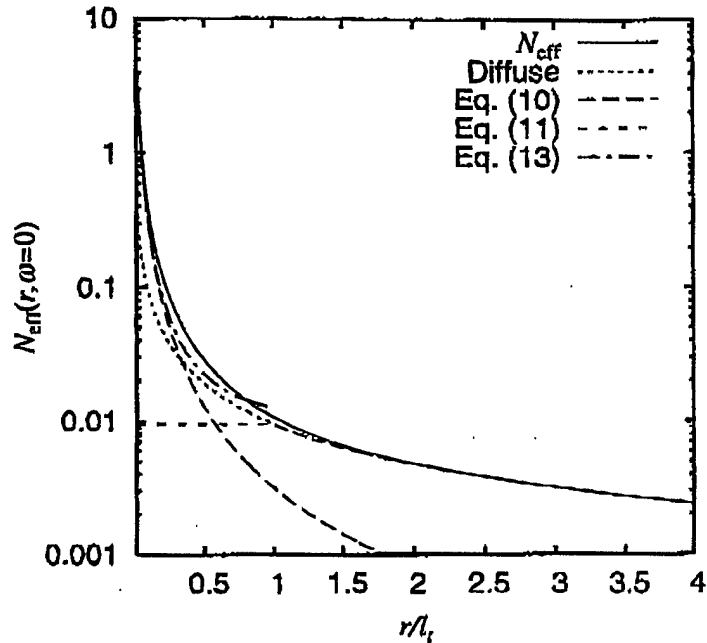
Figure 2. The effective propagator in temporal Fourier space $N_{\text{eff}}(r, \omega = 0)$ for photon migration in a nonabsorbing medium. Its approximations by (14) when $r < l_t$ and by Eq. (11) when $r > l_t$ are also plotted. The diffusion Green's function has a huge error for small r.

See Fig. (3). This difference comes from the fact that Eq. (15) includes the contribution from the ballistic motion of the photon when the photon flies across the site while Eq. (18) does not contain this effect. The former manifests itself in Fig. (3a) as the linear decay of $N_{\text{seff}}(t; R)V$ in the form of $\gamma_0(ct)$ near the origin.

The self-propagator in temporal Fourier space is thus obtained by a temporal Fourier transform of (15):

$$\bar{N}_{\text{self}}(\omega; R) = \int_{0^+}^{+\infty} \bar{N}_{\text{self}}(t; R) \exp(i\omega t) dt \tag{19}$$

$$= \frac{1}{V} \int_0^{2R} dr \gamma_0(r) 4\pi r^2 \int_0^{+\infty} dt N_{\text{eff}}(r, t) \exp(i\omega t)$$

$$= \frac{1}{V} \int_0^{2R} N_{\text{eff}}(r, \omega) \gamma_0(r) 4\pi r^2 dr.$$

The lower limit of integration is 0^+, emphasizing that $t = 0$ should be excluded from integration. Note $\lim_{t \to 0^+} \bar{N}_{\text{eff}}(r, t) = 0$ for our cumulant photon density function. This is not the case for the diffusion Green's function. A numerical quadrature is generally required to compute this self propagator (19). A crude estimation of $\bar{N}_{\text{self}}(\omega; R)$ can be obtained from the asymptotic behavior (11) and (14) of $N_{\text{eff}}(r, \omega)$, i.e.,

$$\bar{N}_{\text{seff}}(\omega; R) \simeq \frac{1}{V} \int_0^{\min(2R, l_t)} \frac{1}{4\pi r^2 c} \exp\left[(i\omega - \mu_a)\frac{r}{c}\right] \gamma_0(r) 4\pi r^2 dr \tag{20}$$

$$+ \frac{1}{V} \int_0^{2R} \frac{1}{8\pi D_\infty r \kappa l_t} \left[\exp(-\kappa |r - l_t|) - \exp(-\kappa(r + l_t))\right] \gamma_0(r) 4\pi r^2 dr.$$
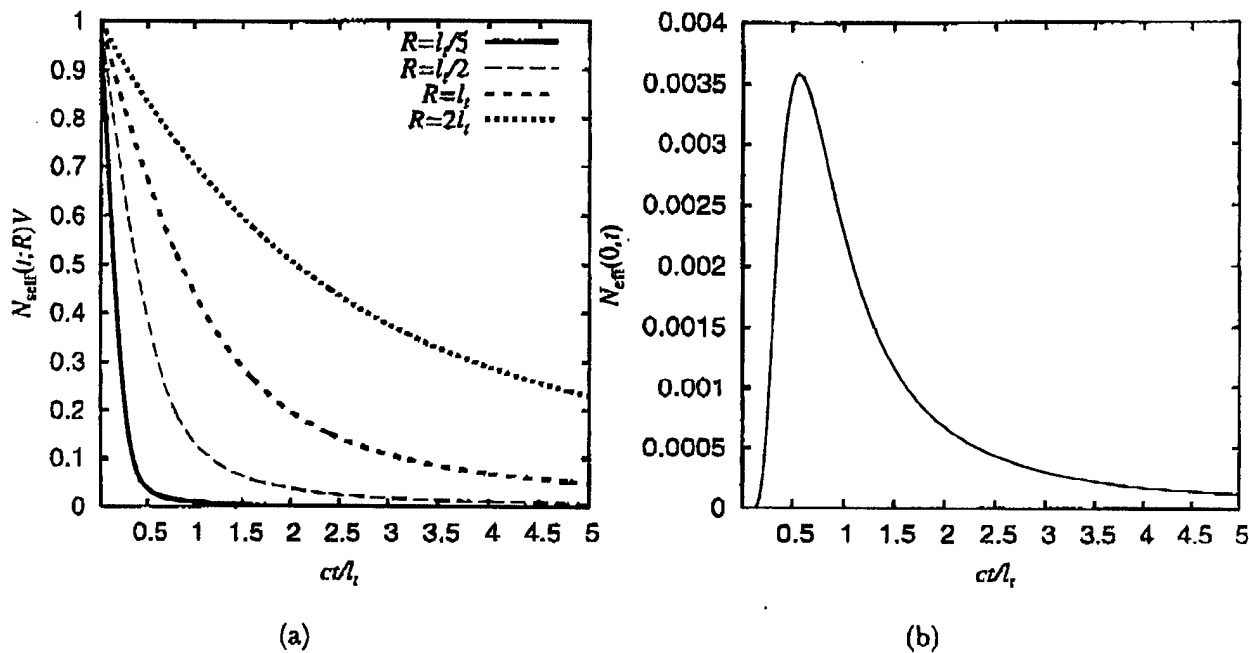
Figure 3. The self-propagators for a finite volume and a point: (a) $N_{\text{self}}(t; R)$ and (b) $N_{\text{eff}}(0, t)$.

This reduces to

$$\bar{N}_{\text{self}}(\omega = 0; R) = \frac{1}{V} \left\{ \begin{array}{ll} \frac{3R}{4c} + \frac{R^3}{l_t^2 c} & R \leq l_t/2 \\ \frac{384R^5 + 160l_t^2 R^3 - 60l_t^3 R^2 + 3l_t^5}{320R^3 l_t c} & R > l_t/2 \end{array} \right. \tag{21}$$

for a continuous wave propagating inside a nonabsorbing medium ($\omega = \mu_a = \kappa = 0$). This estimation turns out to be amazingly good. Fig. (4) plots $\bar{N}_{\text{self}}(\omega = 0; R)$ from numerical quadrature and the crude estimation (21).

3. RESULTS AND DISCUSSION

The multiple passage effect due to the absorption site can now be computed using the self-propagator Eq. (19) derived here. For large sites, the self-propagator $\bar{N}_{\text{self}}(\omega = 0; R)$ increases inverse proportional to its size ($\bar{N}_{\text{self}} \propto R^{-1}$) from Eq. (21); hence the nonlinear correction factor has a form of

$$\frac{1}{1 + \bar{N}_{\text{self}}(\omega; R)V\delta\mu_a(\bar{r})} \simeq \left(1 + \frac{6\delta\mu_a}{5l_t c} R^2 \right)^{-1}, \tag{22}$$

dependent on the area of the absorption site for large R.

Monte Carlo methods have been extensively used in simulation of photon migration.[9, 10] We perform Monte Carlo simulations on a uniform nonabsorbing and isotropic scattering slab (the anisotropic factor of scattering $g = 0$). The units of length of time are chosen such that the mean scattering length $l_s = 1/\mu_s = 1$ and the speed of light $c = 1$. The transport mean free path is hence $l_t = 1$ and the thickness of the slab is assumed $L = 80l_t$. An absorption spherical site is located at the center of the slab $(0, 0, L/2)$ with radius R whose absorption and scattering coefficients are $\mu_{a,2} = \delta\mu_a = 0.01$ and
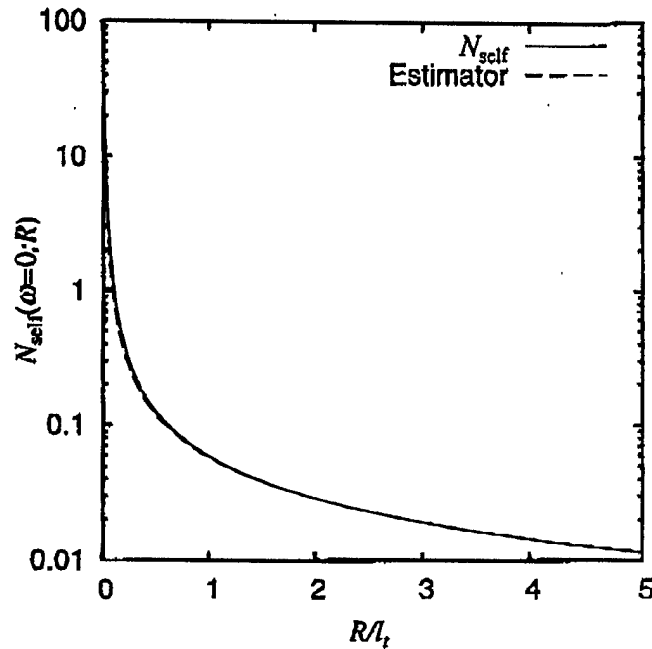
Figure 4. The self propagator $\bar{N}_{\text{self}}(\omega = 0; R)$ and its estimator. The diffusion self-propagator for continuous waves is also plotted.

$\mu_{s,2} = \mu_s$ respectively. The photon is incident at the origin on the left boundary of the slab $z = 0$ in the normal direction of the surface. Each photon is traced until it escapes the slab through either the left or the right boundary. The correlated sampling is used in simulation to reduce variance. A single simulation is used to compute the emitted photon density I_0 for the uniform background (nonabsorption slab) and I for the slab with the absorption site present.

The nonlinear correction factor $[1 + \bar{N}_{\text{self}}(\omega; R)V\delta\mu_a(\bar{r})]^{-1}$ in Eq. (22) can be extracted from the change of the detected light intensity due to the presence of the absorption site in Monte Carlo simulations according to Eq. (2). Fig. (5) plots the theoretical nonlinear correction factor and that from Monte Carlo simulations. "Back" and "Forward" denote the cases where light emits from the left ($z=0$) and the right ($z = L$) boundaries, respectively. The agreement between our theoretical result and Monte Carlo simulations is excellent except for extremely small sizes of inhomogeneities.

Figs. (6) and (7) plot the nonlinear correction factor versus the variation of the modulation frequency of light for a fixed absorption strength and versus the size of the absorption site with a fixed modulation frequency of light respectively. With the increase of the modulation frequency of light, the nonlinear correction becomes less accentuated. The dependence on the size of the inhomogeneity is no longer monotonic for modulated light while the nonlinear correction factor decreases monotonically with the increase of the size for continuous wave light. The phase delay is in the order of a few degrees in the cases investigated.

The typical value of the absorption coefficient of human tissues is around 0.001ps^{-1} while the scattering coefficient is about 1ps^{-1}. Hence the absorption and scattering ratio is in the order of 0.001. This should be compared to our results listed here where the corresponding ratio is 0.01 and one order of magnitude stronger. The nonlinear correction factor for absorption inhomogeneities such as tumors in human tissues is not appreciable unless the size of the inhomogeneity is $R \sim 5l_t$ or larger.
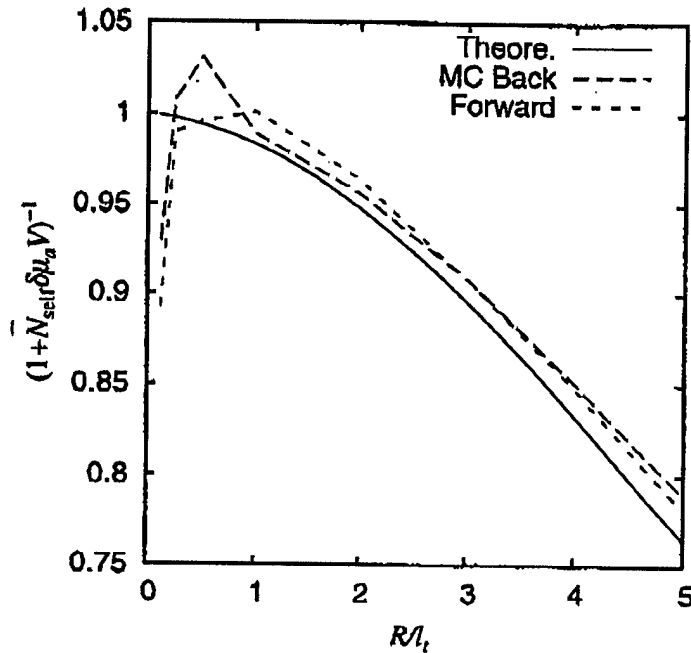
Figure 5. The nonlinear correction factor from the theoretical self-propagator Eq. (19) and Monte Carlo simulations. "Back" and "Forward" denote light emitting from the left ($z=0$)and the right ($z = L$) boundaries. The excess absorption is $\delta\mu_a = 0.01$.
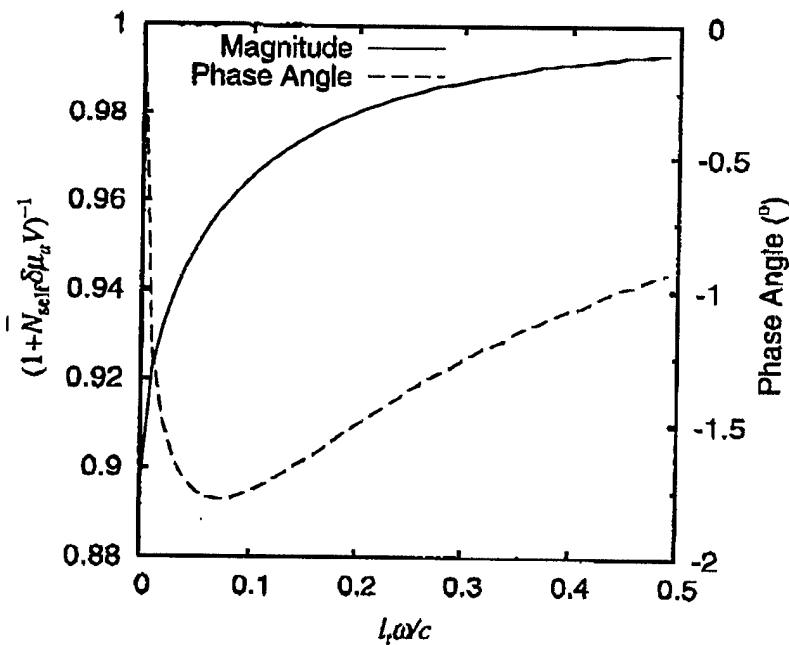

Figure 6. The nonlinear correction factor versus the variation of the modulation frequency of light. The size of the absorption sphere is $R = 3l_t$. The excess absorption is $\delta\mu_a = 0.01$.
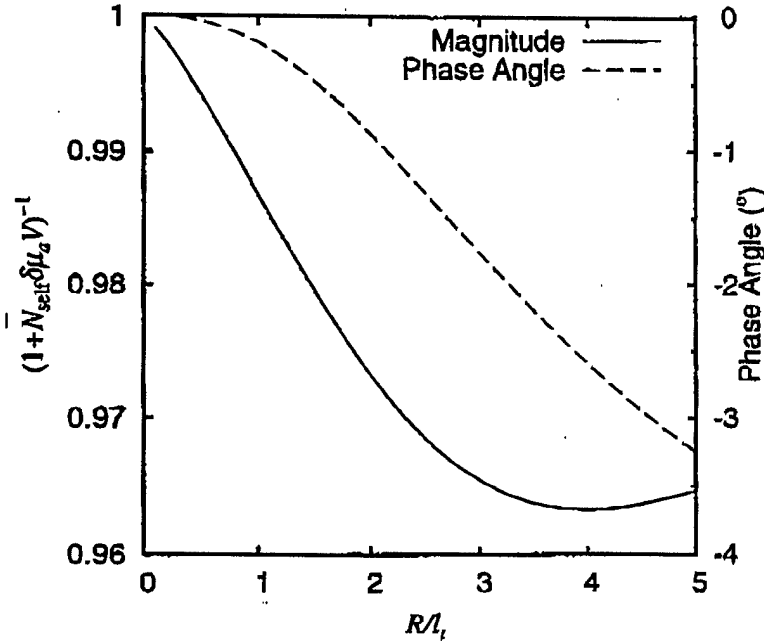
Figure 7. The nonlinear correction factor versus the variation of the size of the absorption site. The modulation frequency of light is $\omega = 0.1$. The excess absorption is $\delta\mu_a = 0.01$.

In conclusion, we have derived an analytical expression for the nonlinear correction factor which agrees well with Monte Carlo simulations. The effect of the nonlinear multiple passage of an absorption site on optical imaging only becomes appreciable when the size of the inhomogeneity is $5l_t$ or larger for human tissues.

APPENDIX A. DERIVATION OF $N_{\mathrm{EFF}}(R,T)$

The spatial Fourier transform of (4) is given by

$$N(\mathbf{k}, t|\mathbf{r}_0, \mathbf{s}_0) = \int d^3\mathbf{r}\, \exp(-i\mathbf{k} \cdot \mathbf{r}) N(\mathbf{r}, t|\mathbf{r}_0, \mathbf{s}_0) = \exp\left(-k^2 D(t)t - \mu_a t - i\mathbf{k} \cdot \mathbf{s}_0 \Delta(t)\right). \quad (23)$$

Hence, the effective propagator in spatial Fourier space at $\mathbf{r}_0$ is expressed as

$$N_{\mathrm{eff}}(\mathbf{k}, t) = \frac{1}{4\pi} \int d^2\mathbf{s}_0 N(\mathbf{k}, t|\mathbf{r}_0, \mathbf{s}_0) = \exp\left(-k^2 D(t)t - \mu_a t\right) \frac{\sin(k\Delta(t))}{k\Delta(t)} \quad (24)$$

by averaging (23) over the propagation direction $\mathbf{s}_0$ of light over the 4π solid angle. The effective propagator in real space is then obtained by an inverse spatial Fourier transform of (24):

$$
\begin{aligned}
N_{\mathrm{eff}}(\mathbf{r}, t) &= \int \frac{d^3\mathbf{k}}{(2\pi)^3} \exp(i\mathbf{k} \cdot \mathbf{r}) \exp\left(-k^2 D(t)t - \mu_a t\right) \frac{\sin(k\Delta(t))}{k\Delta(t)} \\
&= \frac{\exp(-\mu_a t)}{(4\pi)^{3/2}(D(t)t)^{1/2} r\Delta(t)} \left\{ \exp\left[-\frac{(r - \Delta(t))^2}{4D(t)t}\right] - \exp\left[-\frac{(r + \Delta(t))^2}{4D(t)t}\right] \right\} \\
&= \frac{2\exp(-\mu_a t)}{(4\pi)^{3/2}(D(t)t)^{1/2} r\Delta(t)} \exp\left[-\frac{r^2 + \Delta(t)^2}{4D(t)t}\right] \sinh \frac{r\Delta(t)}{2D(t)t}. \quad (25)
\end{aligned}
$$

ACKNOWLEDGMENTS

REFERENCES

1. S. Carraresi, T. S. M. Shatir, F. Martelli, and G. Zaccanti, "Accuracy of a perturbation model to predict the effect of scattering and absorbing inhomogeneities on photon migration," *Appl. Opt.* **40**, pp. 4622–4632, Sept. 2001.

2. M. Xu, W. Cai, M. Lax, and R. R. Alfano, "A transport model for optical tomography in turbid media," in *Signal Recovery and Synthesis*, OSA, 2001.

3. W. Cai, M. Lax, and R. R. Alfano, "Cumulant solution of the elastic Boltzmann transport equation in an infinite uniform medium," *Phys. Rev. E* **61**(4-A), pp. 3871–3876, 2000.

4. M. Xu, W. Cai, M. Lax, and R. R. Alfano, "A photon transport forward model for imaging in turbid media," *Opt. Lett.* **26**(14), pp. 1066–1068, 2001.

5. M. Xu, W. Cai, M. Lax, and R. R. Alfano, "Photon migration in turbid media using a cumulant approximation to radiative transfer," *Phys. Rev. E* **65**, p. 066609, 2002.

6. G. Porod, "Die röntgenkleinwinkelstreuung von dichtgepackten kolloiden systemen i," *Kolloid-Z.* **124**, pp. 83–114, 1951.

7. G. Porod, "Die röntgenkleinwinkelstreuung von dichtgepackten kolloiden systemen ii," *Kolloid-Z.* **125**, pp. 51–57, 109–122, 1952.

8. A. Guinier, G. Fournet, C. B. Walker, and K. L.Yudowitch, *Small-angle scattering of X-rays*, John Wiley & Sons, New York, 1955.

9. A. Sassaroli, C. Blumetti, F. Martelli, L. Alianelli, D. Contini, A. Ismaelli, and G. Zaccanti, "Monte Carlo procedure for investigating light propagation and imaging of highly scattering media," *Appl. Opt.* **37**, pp. 7392–7400, Nov. 1998.

10. M. Testorf, U. sterberg, B. Pogue, and K. Paulsen, "Sampling of time- and frequency-domain signals in monte carlo simulations of photon migration," *Appl. Opt.* **38**, pp. 236–245, January 1999.

Simulated and experimental separation and characterization of absorptive inhomogeneities embedded in turbid media

M. Xu, M. AL-Rubaiee, W. Cai, S. K. Gayen
and R. R. Alfano
Institute for Ultrafast Spectroscopy and Lasers,
New York State Center of Advanced Technology for Ultrafast Photonic Materials
and Applications, and Department of Physics,
The City College and Graduate Center of City University of New York,
New York, NY 10031
minxu@sci.ccny.cuny.edu

Abstract: Independent component analysis of the scattered wave is proposed as the preprocessor to characterization of absorptive inhomogeneities embedded in turbid media. Reconstruction results with simulated and experimental data will be presented for multiple embedded objects.
© 2003 Optical Society of America
OCIS codes: (170.3010) Image reconstruction techniques; (290.7050) Turbid media; (100.3190) Inverse problems

Optical biomedical imaging has attracted significant interests over the past decade because of its potential to noninvasively probe the interior of turbid media such as human breasts.[1, 2, 3] The foreign objects such as tumors inside the turbid medium distort the light flux surrounding the medium. The distortion of the light flux (the scattered wave) can be used to reconstruct the location and the optical properties of the foreign objects via modelling of the light propagation inside the medium.[4] In the linearized scheme of inversion, the perturbation on the light flux due to the inhomogeneity is determined by two Green's functions: the first one $G(\mathbf{r}, \mathbf{r}_s)$ of light propagation from the source at $\mathbf{r}_s$ to the site $\mathbf{r}$ of the inhomogeneity, and the second one $G(\mathbf{r}_d, \mathbf{r})$ of light propagation from the site of inhomogeneity to the detector at $\mathbf{r}_d$. The inverse problem is highly ill-posed because of the smoothing nature of the involved Green's functions. The ill-posedness of the problem is accentuated due to the involvement of both $G(\mathbf{r}, \mathbf{r}_s)$ and $G(\mathbf{r}_d, \mathbf{r})$ in optical imaging.

Recently, independent component analysis (ICA) has been shown to be an effective method to recover unobserved signals (sources) from several observed mixtures.[5, 6] In this report, we propose a novel approach for optical imaging. The distortion of the light exitance is interpreted as a *mixture* of *virtual sources* where the virtual source and the mixing matrix represent the Green's functions $G(\mathbf{r}, \mathbf{r}_s)$ and $G(\mathbf{r}_d, \mathbf{r})$ respectively. The mixing matrix and the virtual sources can be recovered by ICA and used to characterize the embedded inhomogeneities by fitting the individual Green's functions.

Foreign absorptive objects located inside an otherwise uniform infinite slab can be probed using CW (or time-resolved or frequency modulated) scanning point sources. The foreign absorptive objects have an excessive absorption $\delta\mu_a(\mathbf{r})$. Denote the embedded absorption inhomogeneities as $q_i = \delta\mu_a(\mathbf{r}_i)cV_i$ where c is the speed of light in the medium and V_i is the volume of the ith absorption inhomogeneity, the scattered wave field can be written as:

$$-\phi_{\text{sca}}(\mathbf{r}_d; \mathbf{r}_s) = \sum_{j=1}^{n} G(\mathbf{r}_d, \mathbf{r}_j) q_j G(\mathbf{r}_j, \mathbf{r}_s) \tag{1}$$

where $G(\mathbf{r}, \mathbf{r}')$ is the Green's function of the uniform background. The dependence on ω is not explicitly shown as one argument of the Green's function G for clarity.

The scattered wave ϕ_{sca} in (1) hence represents a mixture of n *independent* virtual sources $s_j(\mathbf{r}_s) \equiv q_j G(\mathbf{r}_j, \mathbf{r}_s)$ by the mixing matrix A whose dj entry is $a_j(\mathbf{r}_d) \equiv G(\mathbf{r}_d, \mathbf{r}_j)$, and reduced to the well-known instantaneous mixture model:

$$\mathbf{x}(\mathbf{r}_s) = A\mathbf{s}(\mathbf{r}_s) = \sum_{j=1}^{n} \mathbf{a}_j s_j(\mathbf{r}_s) \tag{2}$$

where

$$\mathbf{x}(\mathbf{r}_s) = (-\phi_{\text{sca}}(\mathbf{r}_{d_1}; \mathbf{r}_s), \dots, -\phi_{\text{sca}}(\mathbf{r}_{d_m}; \mathbf{r}_s))^T \tag{3}$$

$$\mathbf{s}(\mathbf{r}_s) = (s_1(\mathbf{r}_s), \dots, s_n(\mathbf{r}_s))^T$$
$$\mathbf{a}_j = (a_j(\mathbf{r}_{d_1}), \dots, a_j(\mathbf{r}_{d_m}))^T$$
$$A = (\mathbf{a}_1, \dots, \mathbf{a}_n),$$

and $m \geq n$ is the number of sensors. Note the symmetry about the source and the sensors in Eq. (1). The role of sensors and sources can be interchanged freely (the reciprocal property of light propagation). By using the mutual independence among the virtual sources s_j, the virtual sources s_j can be separated up to permutation and scaling. The virtual sources can be extracted simultaneously for all (a parallel scheme) or one by one (a deflation scheme).[5, 7]

After having extracted virtual sources s_j and their corresponding mixing vectors $\mathbf{a}_j$, both the location and strength of the jth object can be computed by a simple fitting procedure. The virtual source s_j and the mixing vector $\mathbf{a}_j$ are the scaled version of the Green's functions $G(\mathbf{r}_j, \mathbf{r}_s)$ and $G(\mathbf{r}_d, \mathbf{r}_j)$ for an absorptive object respectively, i.e.,

$$
\begin{aligned}
s_j &= \alpha_j G(\mathbf{r}_j, \mathbf{r}_s) \\
\mathbf{a}_j &= \beta_j G(\mathbf{r}_d, \mathbf{r}_j).
\end{aligned}
\tag{4}
$$

The location of the jth object $\mathbf{r}_j$ and the strength q_j of the jth object are then obtained by fitting using Eq. (4). The strength of absorption is given by $q_j = \alpha_j \beta_j$.

Fig. (1) displays the separation and characterization of two simulated point absorbers, each of an absorption strength of unity, inside a slab of thickness 50mm. The transport mean free path is 1mm. The incident CW point source scans throughout a set of 21×21 grid points with a spacing of 4.5mm betwen two consecutive grid points on one side of the slab. The light exitance on the other side of the slab is recorded by a CCD camera on twice denser grid points. We used 20% additive Gaussian noise in this simulation. By fitting to Eq. (4), the position of the point absorbers are found to be very close to the input values with an error less than 2mm in all three directions. The strengths of the two unit absorbers are resolved to be 0.98 and 1.01 with an error of less than 2%, respectively.

Fig. (2) shows the result of unmixing of experimental data taken for two parallel absorptive rods immersed inside an Intralipid-10% liquid diluted to have a transport mean free path of 1mm. The thickness of the slab is 50mm and the scanning step is 5mm. The locations are found to be $x = -17.8$mm and $z = 26.4$mm for the first rod, and $x = 14.1$mm and $z = 22.7$mm for the second rod, approximately agreeing with the input values.

This proposed approach is able to locate and reconstruct the optical properties of point inhomogeneities, well suited for the cases of sparse inhomogeneities. In practice, the inhomogeneity of a finite size can be approximated by a point one as long as its dimension is much smaller than the distance from the object to the surface where the light sources and detectors are placed. The same approach can be applied to mixed (absorptive and diffusing) inhomogeneities. The shape of the inhomogeneity may also be estimated by using a similar technique to back-propagation.

References

1. A. Yodh and B. Chance, "Spectroscopy and imaging with diffusing light," Phys. Today **48**, 38–40 (1995).
2. V. Chernomordik, D. Hattery, A. H. Gandjbakhche, A. Pifferi, P. Taroni, A. Torricelli, G. Valentini, and R. Cubeddu, "Quantification by random walk of the optical parameters of nonlocalized abnormalities embedded within tissuelike phantoms," Opt. Lett. **25**, 951–953 (2000).
3. B. A. Brooksby, H. Dehghani, B. W. Pogue, and K. D. Paulsen, "Near-Infrared (NIR) tomography breast image reconstruction with a priori structural information from MRI: algorithm development for reconstructing heterogeneities," IEEE J. Selected Topics in Quantum Electron. **9**, 199–209 (2003).
4. S. R. Arridge, "Optical tomography in medical imaging," Inverse Problems **15**, R41–R93 (1999).
5. P. Comon, "Independent component analysis—a new concept?," Signal Processing **36**, 287–314 (1994).
6. A. J. Bell, "Information Theory, Independent Component Analysis, and Applications," in *Unsupervised Adaptive Filtering, Vol. I*, S. Haykin, ed., (Wiley, 2000), pp. 237–264.
7. A. Hyvärinen, "Fast and robust fixed-point algorithms for independent component analysis," IEEE Trans. on Neural Networks **10**, 626–634 (1999).
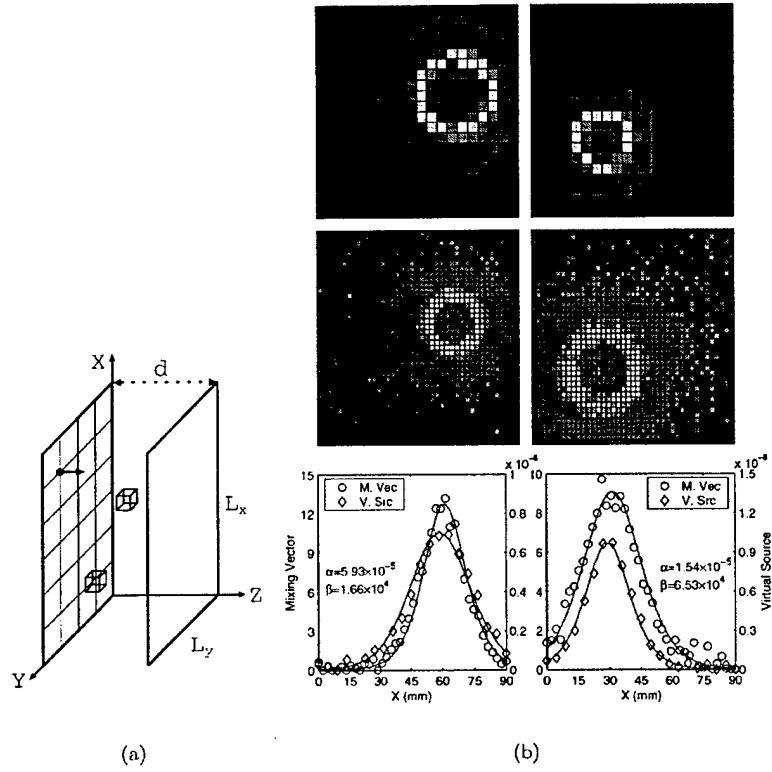
Fig. 1. (a) The setup. (b) The virtual source $(G(\mathbf{r}, \mathbf{r}_s))$, its mixing vector $(G(\mathbf{r}_d, \mathbf{r}))$ and the fitting to Eq. (4). The left column is for the first point source at $(50, 60, 30)$mm and the right column is for the second point source at $(30, 30, 20)$mm.
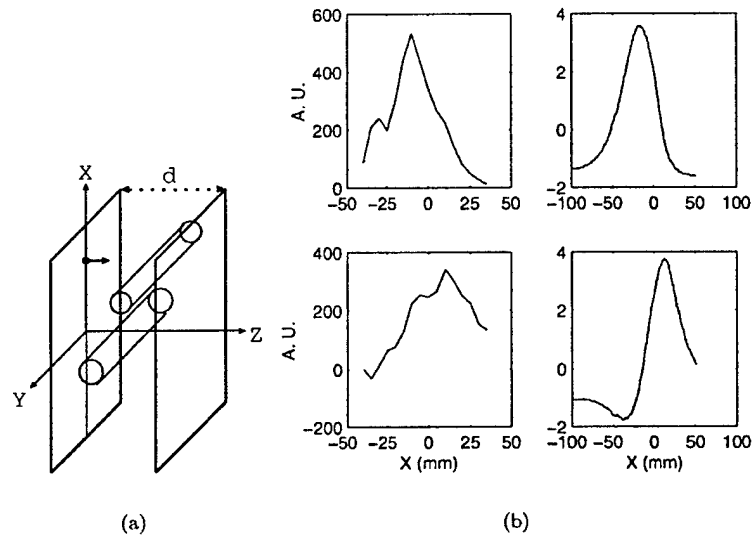

Fig. 2. (a) The setup. (b) The virtual sources $(G(\mathbf{r}, \mathbf{r}_s))$ and the mixing vectors $(G(\mathbf{r}_d, \mathbf{r}))$ for the first rod (the upper row) and the second rod (the lower row).

Multiple passages of light through an absorption inhomogeneity in optical imaging of turbid media

M. Xu, W. Cai, and R. R. Alfano

Institute for Ultrafast Spectroscopy and Lasers, New York State Center of Advanced Technology for Ultrafast Photonic Materials and Applications, and Department of Physics, The City College and Graduate Center of the City University of New York, New York, New York 10031

Multiple passages of light through an absorption inhomogeneity of finite size deep within a turbid medium are analyzed for optical imaging by use of the self-energy diagram. The nonlinear correction becomes more important for an inhomogeneity of a larger size and with greater contrast in absorption with respect to the host background. The nonlinear correction factor agrees well with that from Monte Carlo simulations for cw light. The correction is approximately 50%–75% in the near infrared for an absorption inhomogeneity with the typical optical properties found in tissues and five times the size of the transport mean free path. © 2004 Optical Society of America

OCIS codes: 290.4210, 290.7050, 170.3660.

The main objective of optical imaging of turbid media is to locate and identify the embedded inhomogeneities by essentially inverting the difference in photon transmittance in the time or frequency domains due to the presence of these inhomogeneities.[1-4] The key quantity involved is the Jacobian, which quantifies the influence on the detected signal due to the change of the optical parameters of the medium. The linear perturbation approach is suitable for calculating the Jacobian for only a small and weak absorption inhomogeneity and is not valid when the absorption strength is large.[5] This failure can be attributed to the multiple passages through the abnormal site by the photon. The most important correction is the self-energy correction,[6] which takes into account the repeated visits made by a photon through the site up to an infinite number of times. The presence of other inhomogeneity islands can be ignored because the photon propagator decreases rapidly with the distance between two separate sites.

In this Letter the nonlinear correction for an absorption inhomogeneity of a large strength due to repeated visits by the photon is modeled by a nonlinear correction factor (NCF) to the linear perturbation approach. The NCF as a function of the size and the strength of the inhomogeneity is estimated by use of the self-energy diagram. The NCF is obtained from the cumulant approximation to the radiative transfer and verified by Monte Carlo simulations for cw light. The magnitude of the NCF is 0.5–1 for an absorptive inhomogeneity of up to $5l_t$ (l_t is the mean transport free path of light) and of the typical optical properties of human tissues ($\mu_a l_t/c \sim 0.01$–0.05, where μ_a is the absorption coefficient and c is the speed of light in the medium).

If we consider an absorption site centered at $\overline{\mathbf{r}}$ and far away from both the source and the detector, the change in the detected light ΔI at the detector $\mathbf{r}_d$ from a modulated point source at $\mathbf{r}_s$ including the multiple passages through the site is given by

$$\Delta I = -G(\mathbf{r}_d, \omega \mid \overline{\mathbf{r}})V\delta\mu_a(\overline{\mathbf{r}})\sum_{n=0}^{\infty}[-\overline{N}_{\text{self}}(\omega; R)V\delta\mu_a(\overline{\mathbf{r}})]^n$$

$$\times\, G(\overline{\mathbf{r}}, \omega \mid \mathbf{r}_s)$$

$$= -G(\mathbf{r}_d, \omega \mid \overline{\mathbf{r}})\frac{V\delta\mu_a(\overline{\mathbf{r}})}{1 + \overline{N}_{\text{self}}(\omega; R)V\delta\mu_a(\overline{\mathbf{r}})}$$

$$\times\, G(\overline{\mathbf{r}}, \omega \mid \mathbf{r}_s),\tag{1}$$

where $\delta\mu_a$ is the excess absorption of the absorption site of size R and volume V, ω is the modulation frequency of light, G is the propagator of photon migration in the background medium, and

$$\overline{N}_{\text{self}}(\omega; R) = \frac{1}{V^2}\int_V\int_V G(\mathbf{r}_2, \omega \mid \mathbf{r}_1)\mathrm{d}^3\mathbf{r}_2\mathrm{d}^3\mathbf{r}_1\tag{2}$$

is the self-propagator that describes the probability that a photon revisits volume V. Here $G(\mathbf{r}_2, \omega \mid \mathbf{r}_1)$ gives the probability density that a photon leaves the volume at $\mathbf{r}_1$ and re-enters it at $\mathbf{r}_2$. The scattering property of the site is the same as that of the background. In Eq. (1) $G(\mathbf{r}_d, \omega \mid \overline{\mathbf{r}})$ and $G(\overline{\mathbf{r}}, \omega \mid \mathbf{r}_s)$ are well modeled by the center-moved diffusion model as long as separations $|\mathbf{r}_d - \overline{\mathbf{r}}|$ and $|\mathbf{r}_s - \overline{\mathbf{r}}|$ are much greater than l_t.[7] However, the diffusion Green's function cannot be used in Eq. (2) to evaluate $\overline{N}_{\text{self}}(\omega; R)$ because the diffusion approximation breaks down when $\mathbf{r}_1$ is in the proximity of $\mathbf{r}_2$.

Comparing Eq. (1) with the standard linear perturbation approach, the nonlinear multiple passage effect of an absorption site is represented by a NCF:

$$\text{NCF} = [1 + \overline{N}_{\text{self}}(\omega; R)V\delta\mu_a(\overline{\mathbf{r}})]^{-1}.\tag{3}$$

This factor serves as a universal measure of the nonlinear multiple-passage effect as long as the absorption site is far from both the source and the detector and its size is much smaller than its distance to both the source and the detector. This correction is more significant when the NCF is further away from unity.

Photon propagator $N(\mathbf{r}_2, t \,|\, \mathbf{r}_1, \mathbf{s})$, the probability that a photon propagates from position $\mathbf{r}_1$ with propagation direction $\mathbf{s}$ to position $\mathbf{r}_2$ in time t, for any separation between $\mathbf{r}_1$ and $\mathbf{r}_2$, was recently derived[7,8] in a form of the cumulant approximation to the radiative transfer.

In the case of interest in which the absorption site is deep inside the medium, the photon distribution is isotropic. The photon propagator is simplified to $N_{\mathrm{eff}}(r, t) \equiv N_{\mathrm{eff}}(|\mathbf{r}_2 - \mathbf{r}_1|, t)$, which is obtained by averaging $N(\mathbf{r}_2, t \,|\, \mathbf{r}_1, \mathbf{s})$ over the propagation direction $\mathbf{s}$ of light over the 4π solid angle. In the frequency domain this effective propagator is approximately given by

$$N_{\mathrm{eff}}(r, \omega) \simeq \begin{cases} \dfrac{1}{4\pi r^2 c} \exp\!\left(-\dfrac{1}{3}\kappa^2 l_t r\right) \\[2mm] \quad + \dfrac{\exp(-\kappa l_t)}{4\pi D r \kappa l_t}\sinh(\kappa r), & r < l_t \\[3mm] \dfrac{\exp(-\kappa r)}{4\pi D r \kappa l_t}\sinh(\kappa l_t), & r \geq l_t \end{cases} \quad (4)$$

where $D \equiv l_t c/3$ and $\kappa \equiv [3(\mu_a - i\omega)/l_t c]^{1/2}$, whose sign is chosen with a nonnegative real part. The two terms in N_{eff} when $r < l_t$ represent ballistic and diffusion contributions, respectively. The ballistic term does not depend on scattering because the photon distribution involved is already isotropic. Only diffusion contributes to N_{eff} when $r > l_t$. The self-propagator for an absorption sphere deep inside the medium is given by

$$\overline{N}_{\mathrm{self}}(\omega; R) = \frac{1}{V^2}\int_V\int_V N_{\mathrm{eff}}(|\mathbf{r}_2 - \mathbf{r}_1|, \omega)\,d^3 r_2\,d^3 r_1$$

$$= \frac{1}{V}\int_0^{2R} N_{\mathrm{eff}}(r, \omega)\gamma_0(r)4\pi r^2\,dr, \quad (5)$$

where $\gamma_0(r) = 1 - (3r/4R) + (1/16)(r/R)^3$ is the characteristic function for a uniform sphere.[9] An absorption site of an arbitrary shape can be treated the same way. The exact self-propagator must be computed by a numerical quadrature. A good approximation of $\overline{N}_{\mathrm{self}}(\omega; R)$ is

$$\overline{N}_{\mathrm{self}}(\omega; R) = \frac{l_t}{Vc}$$

$$\times \begin{cases} \left(\dfrac{3}{4}\xi + \xi^3\right) - \xi^3\kappa l_t + \mathcal{O}(\kappa^2), & \xi \leq 1/2 \\[3mm] \left(\dfrac{6}{5}\xi^2 + \dfrac{1}{2} - \dfrac{3}{16}\xi^{-1} + \dfrac{3}{320}\xi^{-3}\right) \\[3mm] \quad -\xi^3\kappa l_t + \mathcal{O}(\kappa^2), & \xi > 1/2 \end{cases} \quad (6)$$

by use of relation (4), where $\xi \equiv R/l_t$ when $|\kappa|R \ll 1$. The exact and approximate versions of dimensionless self-propagator $\overline{N}_{\mathrm{self}}Vl_t^{-1}c$ when $\kappa = 0$ are plotted as solid and dashed curves, respectively, in Fig. 1(a). Dimensionless self-propagator $\overline{N}_{\mathrm{self}}Vl_t^{-1}c$ depends solely on two dimensionless quantities κl_t of the background and R/l_t of the absorbing sphere.

It is worthwhile to point out that self-propagator in time $\overline{N}_{\mathrm{self}}(t; R)$, the inverse Fourier transform of

Eq. (5), includes the contribution from the ballistic motion of the photon when the photon passes through the site. This ballistic contribution manifests itself as the linear decay of $N_{\mathrm{self}}(t; R)V$ in the form of $\gamma_0(ct)$ near the origin of the time, followed by a transition to diffusion [Fig. 1(b)].

The NCF is obtained by plugging Eq. (5) or (6) into Eq. (3). In particular, we have

$$\mathrm{NCF} \simeq \begin{cases} \left[1 + \dfrac{9}{16\pi}q\left(\xi^{-2} + \dfrac{4}{3}\right)\right]^{-1}, & \xi \leq 1/2 \\[3mm] \Big[1 + \dfrac{9}{10\pi}q\Big(\xi^{-1} + \dfrac{5}{12}\xi^{-3} \\[3mm] \quad - \dfrac{5}{32}\xi^{-4} + \dfrac{1}{128}\xi^{-6}\Big)\Big]^{-1}, & \xi > 1/2 \end{cases} \quad (7)$$

where $q \equiv V\delta\mu_a(\mathbf{r})/l_t^2 c$ is the dimensionless strength of the absorber when $|\kappa|R \ll 1$. For an absorber of fixed $q > 0$, the effectiveness of absorbing light is diminished (the NCF decreases) when its size is reduced. This can be understood from the fact that the photon spends less time per volume inside the absorber of a smaller dimension because of the ballistic motion of the photon after each scattering event. The photon leaves a small site ($R < l_t$) in an almost straight line. The diffusion behavior for an individual photon is observed only after a large number of scattering and on a scale larger than l_t.

Figure 2 shows plots of the NCF versus absorber size for typical absorbers of excess absorption $\delta\mu_a l_t/c$ equal to 0.01 and 0.05. The nonlinear correction factor generally decreases with the size of the absorber whose excess absorption is fixed. With the increase of the background absorption and the modulation frequency, the nonlinear correction becomes less accentuated. The phase delay is larger for higher modulation frequencies and less background absorption.

Monte Carlo simulations[10] are performed for cw light propagating in a uniform nonabsorbing and isotropic scattering slab. The thickness of the slab is $L = 80 l_t$. A spherical absorber of radius R is located at the center $(0, 0, L/2)$ of the slab. The excess absorption of the absorber is $\delta\mu_a l_t/c = 0.01$. The absorber has the same scattering property as the background. The details of the Monte Carlo computation were provided in a previous publication.[11] The correlated sampling method
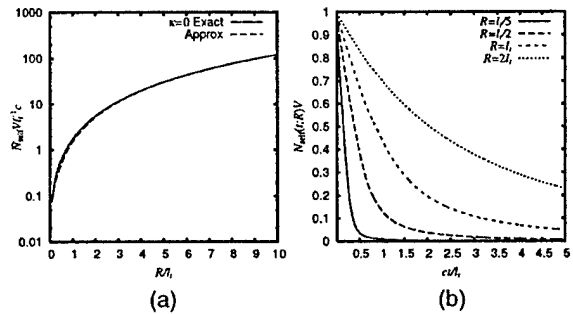

Fig. 1. (a) Self-propagator $\overline{N}_{\mathrm{self}}(\omega; R)Vl_t^{-1}c$ and its approximation form when $\kappa = 0$. (b) Self-propagator for spheres of various radii in the time domain inside a nonabsorbing medium.
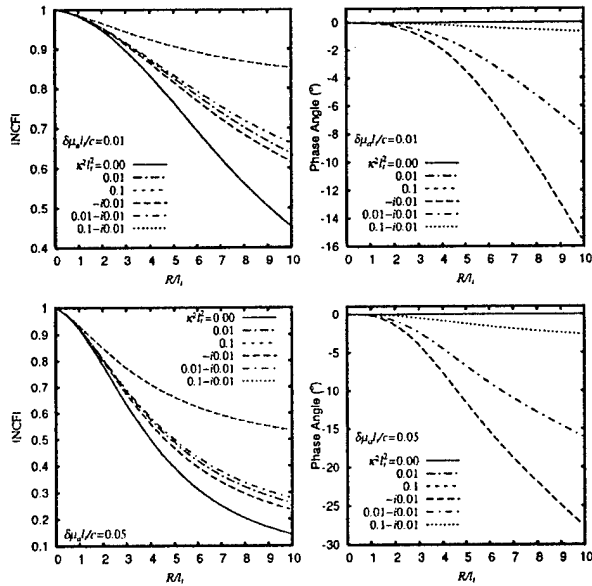
(ms #18662a/irm)

Fig. 2. NCF (magnitude and phase angle) versus the size of absorbers whose excess absorption $\delta\mu_a l_t/c$ equals 0.01 and 0.05. Note that $\kappa^2 l_t^2 = 3(\mu_a - i\omega)l_t/c$ for the background medium.
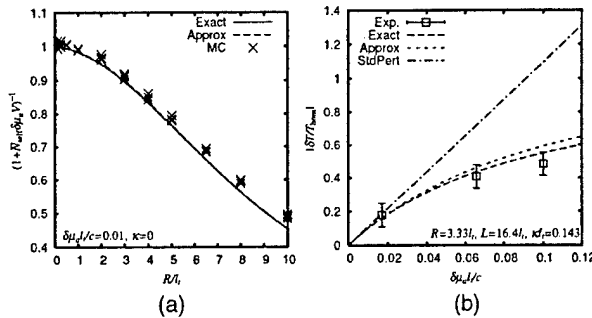

Fig. 3. (a) Theoretical nonlinear correction factors from numerical quadrature (Exact), the approximate form of relation (7) (Approx), and Monte Carlo simulations (MC). Results from four independent Monte Carlo simulations are shown for each radius. The standard linear perturbation approach corresponds to horizontal line NCF = 1 (not shown in the figure). (b) Percentage change of the cw transmittance from the experimental data given in Fig. 9 of Ref. 5 compared with the theoretical predictions made by the standard linear perturbation approach (StdPert) and those including NCF (Exact and Approx).

is used in each simulation to reduce variance.[12] A single simulation is used to compute the change in light transmittance due to the presence of the absorption site and the corresponding NCF. Figure 3(a) shows the NCFs obtained from numerical quadrature, the approximate form of relation (7), and Monte Carlo simulations. The agreement between our theoretical NCF and that from Monte Carlo simulations is excellent. The slight difference between them at large radii is accounted for by the fact that the sphere can no longer be regarded as small compared with the dimensions of the slab. The probability of a photon revisiting a large sphere is overestimated by Eq. (5) for the sphere located at the center of the slab.[13]

Figure 3(b) shows the percentage change of the cw transmittance estimated from the experimental data given in Fig. 9 of Ref. 5. The relevant parameters of the experiment are summarized in the inset. The theoretical predictions from the linear perturbation approach with and without the nonlinear correction are also shown in Fig. 3(b), assuming a collimated point source and a point detector in a confocal setup. Our theoretical prediction with nonlinear correction provides a significant improvement over linear perturbation and agrees much better with the experimental result.

The typical value of the absorption coefficient of human tissues in the near infrared indicates that $\mu_a l_t/c \sim 0.01$–0.05.[14,15] This fact should put our results on NCFs in this range (Figs. 2 and 3) into perspective. The nonlinear correction becomes more important for an inhomogeneity of a larger size and with greater contrast in absorption with respect to the background. The value of the NCF decreases from ~ 0.75 to ~ 0.5 for an absorption site of radius $5l_t$ with excess absorption $\delta\mu_a l_t/c$ increasing from 0.01 to 0.05. The standard linear perturbation approach in optical imaging should be augmented to include this nonlinear correction.

References

1. A. Yodh and B. Chance, Phys. Today 48(3), 38 (1995).
2. S. R. Arridge, Inverse Probl. 15, R41 (1999).
3. A. H. Gandjbakhche, V. Chernomordik, J. C. Hebden, and R. Nossal, Appl. Opt. 37, 1973 (1998).
4. W. Cai, S. K. Gayen, M. Xu, M. Zevallos, M. Alrubaiee, M. Lax, and R. R. Alfano, Appl. Opt. 38, 4237 (1999).
5. S. Carraresi, T. S. M. Shatir, F. Martelli, and G. Zaccanti, Appl. Opt. 40, 4622 (2001).
6. J. W. Negele and H. Orland, *Quantum Many-Particle Systems* (Westview, Boulder, Colo., 1998).
7. M. Xu, W. Cai, M. Lax, and R. R. Alfano, Opt. Lett. 26, 1066 (2001).
8. W. Cai, M. Lax, and R. R. Alfano, Phys. Rev. E 61, 3871 (2000).
9. A. Guinier, G. Fournet, C. B. Walker, and K. L. Yudowitch, *Small-Angle Scattering of X-Rays* (Wiley, New York, 1955).
10. M. Testorf, U. Osterberg, B. Pogue, and K. Paulsen, Appl. Opt. 38, 236 (1999).
11. M. Xu, W. Cai, M. Lax, and R. R. Alfano, Phys. Rev. E 65, 066609 (2002).
12. H. Rief, J. Comput. Phys. 111, 33 (1994).
13. Consider the facts that (1) the probability of a photon revisiting the sphere decreases when the position from which the photon leaves the sphere is further away from the center of the sphere and (2) the photon density inside the sphere is higher in regions closer to its surface for the sphere located at the center of the slab. The arithmetic mean taken in Eq. (5) hence overestimates the revisiting probability.
14. V. G. Peters, D. R. Wyman, M. S. Patterson, and G. L.

Frank, Phys. Med. Biol. **35,** 1317 (1990).
15. W. F. Cheong, S. Prahl, and A. J. Welch, IEEE J. Quantum Electron. **26,** 2166 (1990).